A monthly 1-degree resolution dataset of cloud fraction over the Arctic during 2000–2020 based on multiple satellite products

Xinyan Liu[1], Tao He[1], Shunlin Liang[2], Ruibo Li[3], Xiongxin Xiao[4], Rui Ma[1], Yichuan Ma[1]

[1] School of Remote Sensing and Information Engineering, Wuhan University, Wuhan 430079, China

[2] Department of Geography, University of Hong Kong, Hong Kong 999077, China

[3] State Key Laboratory of Remote Sensing Science, Aerospace Information Research Institute, Chinese Academy of Sciences, Beijing 100101, China

[4] Institute of Geography and Oeschger Center for Climate Change Research, University of Bern, Bern 3012, Switzerland

Correspondence to: Tao He (taohers@whu.edu.cn)

Abstract. The low accuracy of satellite cloud fraction (CF) data over the Arctic seriously restricts the accurate assessment of the regional and global radiative energy balance under a changing climate. Previous studies have reported that no individual satellite CF product could satisfy the needs of accuracy and spatio-temporal coverage simultaneously for long-term applications over the Arctic. Merging multiple CF products with complementary properties can provide an effective way to produce a spatiotemporally complete CF data record with higher accuracy. This study proposed a spatiotemporal statistical data fusion framework based on cumulative distribution function (CDF) matching and the Bayesian maximum entropy (BME) method to produce a synthetic $1°\times1°$ CF dataset in the Arctic during 2000–2020. The CDF matching was employed to remove the systematic biases among multiple passive sensor datasets through the constraint of using CF from an active sensor. The BME method was employed to combine adjusted satellite CF products to produce a spatiotemporally complete and accurate CF product. The advantages of the presented fusing framework are that it not only uses the spatiotemporal autocorrelations but also explicitly incorporates the uncertainties of passive sensor products benchmarked with reference data, i.e., active sensor product and ground-based observations. The inconsistencies of Arctic CF between passive sensor products and the reference data were reduced by about 10–20% after fusing, with particularly noticeable improvements in the vicinity of Greenland. Compared with ground-based observations, R^2 increased by about 0.20–0.48 and the root mean square error (RMSE) and bias reductions averaged about 6.09% and 4.04% for land regions, respectively; these metrics for ocean regions were about 0.05–0.31, 2.85%, and 3.15%, respectively. Compared with active sensor data, R^2 increased by nearly 0.16, and RMSE and bias declined by about 3.77% and 4.31%, respectively, in land; meanwhile, improvements in ocean regions were about 0.3 for R^2, 4.46% for RMSE and, 3.92% for bias. The results of the comparison with the ERA5 and the MRI-AGCM3-2-S climate model suggest an obvious improvement in the consistency between the satellite-observed CF and the reanalysis and model data after fusion. This serves as a promising indication that the fused CF results hold the potential to deliver reliable satellite observations for modeling and reanalysis data. Moreover, the fused product effectively supplements the temporal gaps of AVHRR-based products caused by satellite faults and the data missing from MODIS-based products prior to the launch of Aqua, and extends

the temporal range better than the active product; it addresses the spatial insufficiency of the active sensor data and the AVHRR-based products acquired at latitudes greater than 82.5 °N. A continuous monthly 1-degree CF product covering the entire Arctic during 2000–2020 was generated and is freely available to the public at https://doi.org/10.5281/zenodo.7624605 (Liu et al., 2022). This is of great importance for reducing the uncertainty in the estimation of surface radiation parameters and thus helps researchers to better understand the earth's energy imbalance.

1 Introduction

Clouds substantially affect Earth's energy budget by reflecting solar radiation back to space and by restricting emissions of thermal radiation into space (Ramanathan et al., 1989; Van Tricht et al., 2016; Danso et al., 2020). Clouds are also an essential variable in the climate system because they are directly associated with precipitation and aerosol loading (Toll et al., 2019; Poulsen et al., 2016). The cloud fraction (CF), which represents the amount of sky estimated to be covered by a specified cloud type or level (partial CF) or by all cloud types and levels (total CF), has long been recognized as a major source of uncertainty when estimating radiation flux and future climate change (Xie et al., 2010; Liu et al., 2011a; Qian et al., 2012; Danso et al., 2020). An accurate representation of CF is essential for the evaluation of regional and global energy budgets as well as for predicting future climatic conditions. However, variances in CF definitions and system differences commonly exist among different sources of data. As a solution, the fused product provides a higher level of definition consistency and accuracy in comparison to alternative datasets.

By making spatially continuous observations, satellites provided us with an unprecedented advantage in assessing regional and global cloud effects. In the last few decades, increased effort has been made to develop, analyze, and validate global or regional cloud property datasets that are based on long-term satellite observations (Heidinger et al., 2014; Hollmann et al., 2013; Karlsson and Devasthale, 2018; Marchant et al., 2016; Rossow and Schiffer, 1999; Stubenrauch et al., 2013; Enriquez-Alonso et al., 2016; Sun et al., 2015; Tzallas et al., 2019; Wu et al., 2014). Studies have also shown that although different cloud datasets were derived from different observation instruments and algorithms, most of them provide quite consistent CF observations in middle and lower-latitude regions (Karlsson and Devasthale, 2018; Stengel et al., 2017; Claudia, 2012). However, systematic errors and artifacts exist in CF data, so some inconsistencies inevitably occur among different datasets (Sun et al., 2015; Tzallas et al., 2019; Wu et al., 2014), especially in the polar regions (Liu et al., 2022). Perennial snow/ice coverage coupled with frequent moisture inversions in Arctic has limited the cloud detection capabilities of passive sensor datasets, where the differences between these various datasets tend to be about two-fold in magnitude when compared with datasets acquired at other latitudes (Karlsson and Devasthale, 2018; Liu et al., 2022; Stubenrauch et al., 2013). The uncertainties of the annual global surface downward longwave (LW) and shortwave (SW) fluxes caused by satellite-derived cloud properties were calculated at about 2% (7 Wm^{-2} and 4 Wm^{-2}, respectively) and those for global surface upward LW and SW were about 0.8% (about 3 Wm^{-2}) and 13% (also 3 Wm^{-2}), respectively (Kato et al., 2011; Kato et al., 2012; Kim and Ramanathan, 2008). It should be noted that the differences in CF may have a more obvious impact on the surface radiation budget in high-latitude polar regions. Kennedy et al. (2012) found that the CF bias might cause monthly biases in Arctic surface SW and LW fluxes over 90 and 60 Wm^{-2} for some reanalyses, respectively (Kennedy et al., 2012). Walsh et al. (2009) proposed that the bias of summer low-level CF would create deviations of about 160 Wm^{-2} in estimated SW radiation (Walsh et al., 2009).

Some other related studies have also found that the variances of annual Arctic surface radiation estimation caused by CF uncertainty were higher than $10\,\mathrm{Wm^{-2}}$ (Hakuba et al., 2017; Kato et al., 2018b; Huang et al., 2017). Therefore, relying on a single CF dataset may introduce large uncertainty when analyzing the cloud dynamics over the Arctic, further affecting the estimated energy budget and related climate applications.

Each cloud dataset has its own advantages and disadvantages in Arctic CF detection. The Advanced Very High Resolution Radiometer (AVHRR) offers the longest continuous satellite observation records extending from 1978 to the present and provides daily global coverage based on data from several AVHRRs. With the successful operation of new generations of satellites, the frequency of global view has increased to more than eight each day, which provides richer angular information for CF observations (Heidinger et al., 2014; Karlsson et al., 2017). Many cloud products exist that are based on AVHRR sensors. The International Satellite Cloud Climatology Project (ISCCP) H-series product relies on newer passive imagers with higher spectral, spatial, radiometric, and temporal resolutions; it provides revised daytime cloud detection over snow and ice in polar regions (Young et al., 2018). Moreover, the ISCCP is largely unaffected by the AVHRR orbital drifts (Loyola R et al., 2010; Liu et al., 2022). The CM SAF cLoud, Albedo, and RAdiation datasets (CLARA-A1/A2) systematically use CALIPSO-CALIOP cloud information for development and validation purposes, and it optimizes the detection conditions during the polar day over snow- and ice-covered surfaces (Karlsson et al., 2017; Karlsson and Hakansson, 2018). The AVHRR Pathfinder Atmospheres - Extended (PATMOS-x) product is the first multi-parameter dataset that is making use of all AVHRR channels. This product has a relatively finer spatial resolution than other AVHRR-based records, and it also improves cloud detection based on active sensor data (Heidinger et al., 2012; Heidinger et al., 2014). However, the AVHRR-based products are often reported to underestimate Arctic CF because of the limitations in radiation correction and spatial bands (Stengel et al., 2017; Kotarba, 2015). In addition, the United States National Oceanic and Atmospheric Administration's (NOAA's) archiving of data has its own problems with intermittent occurrences of gaps, duplications, and corrupt data as well as the orbit drifts of satellites (Karlsson et al., 2017). Beginning in 2000, the higher resolution, higher calibration accuracy, and larger number of spectral bands used in the Moderate Resolution Imaging SpectroRadiometer (MODIS) cloud products resulted in more robust, but shorter-length products than AVHRR (Kennedy et al., 2012; Claudia, 2012; Stengel et al., 2017), including MOD08/MYD08 (Marchant et al., 2016) and the Clouds and the Earth's Radiant Energy System (CERES) (Kato et al., 2018b; Minnis et al., 2011). Meanwhile, the MODIS-based products are usually reported to overestimate the CF in the Arctic (Trepte et al., 2019; Liu et al., 2022). Although passive sensor data provide a long time series of continuous CF data covering the entire Arctic region, the limitations of visible and thermal channels in distinguishing clouds from snow and ice cause the cloud results of passive sensor data in the high-latitude bright cold polar regions to have questionable accuracy (Eastman and Warren, 2010; Liu et al., 2010; Liu et al., 2012a; Philipp et al., 2020). Active instruments, such as CALIOP, do not rely on thermal or visible contrasts in detecting clouds, so they are regarded as an excellent reference for passive data collection in transient and zonular scenarios (Stubenrauch et al., 2013; Stengel et al., 2017). However, the number of CALIPSO spatial samplings is too low to overlap large areas repeatedly in a short time, and the CALIPSO imagers only cover the regions within 82.5°N latitudes, which greatly reduced spatial and temporal coverages when compared with passive sensor sensors (Liu et al., 2022; Claudia, 2012; Stubenrauch et al., 2013). Moreover, differences in instrumentation impose these different cloud definitions, which further larged the biases between the passive sensor data and the active sensor data. Therefore, an effective method for blending the advantages

126 of multiple satellite products should yield more accurate Arctic CF products based on a variety of
127 observations and algorithms.

128   Several studies have been dedicated to correcting passive sensor data based on active sensor data
129 with the goal of improving the accuracy of CF products. Philipp et al. (2020) corrected passive sensor
130 CF data by constructing a function of the sea ice concentration in different seasons and the CF bias in
131 data acquired from active and passive sensors, which showed reliable results for low-level cloud cover
132 identification where the sea ice concentration was known (Philipp et al., 2020). Kotarba (2020) matched
133 the CALIPSO profile data and the MODIS instantaneous field of view to correct passive sensor data
134 (Kotarba, 2020). This method can be used as an important reference for short-term research that focused
135 a small area, while the efficiency of the algorithm is also important for the correction of long-time series
136 and large-scale data. Given that passive sensor CFs exhibit seasonal fluctuations similar to those of active
137 sensor data (peaking in September and minimizing in April in the Arctic), an approach based on
138 cumulative distribution function (CDF) matching using time series data may be able to improve both the
139 accuracy and efficiency of CF detection. Using CDF matching can reduce the systematic bias and root
140 mean square errors (RMSEs) between target and reference datasets while maintaining the relative
141 relationship, which has been successfully applied in the study of soil moisture, surface emissivity spectra,
142 precipitation, and land surface temperature (Drusch, 2005; Brocca et al., 2011; Liu et al., 2011b; Zhang
143 et al., 2018; Nie et al., 2016; Xu and Cheng, 2021).

144   In the field of meteorology, to obtain more accurate cloud coverage information, multi-source data
145 fusion is usually performed based on spectral bands and scale geometry information of instantaneous
146 satellite images. Examples include various transforms including the contourlet(Miao and Wang, 2006;
147 Jin et al., 2011), curvelet (Li and Yang, 2008; Liu et al., 2015), NSCT (Wang et al., 2012), and tetrolet
148 transforms (Zhang et al., 2014). Alternatively, based on the field of view of different observation
149 instruments used to acquire satellite images and of ground-based stations, methods such as the stepwise
150 revision method (Kenyon et al., 2016) and data assimilation technology (Hu and Xue, 2007) have been
151 used. However, in the climate domain, the estimation of a radiative energy budget on a large scale over
152 a long time series usually requires monthly climate model grid data (Kato et al., 2018a; Sledd and
153 L'ecuyer, 2021). Using fused instantaneous data to extrapolate climate-scale data may result in a large
154 accumulation of errors. In recent decades, the fusion of multi-sensor thematic products in climate-scale
155 studies has been widely used and developed. Two main types of methods exist for merging multiple
156 satellite thematic products based on the principle of calculation. One type of fusing approach provides
157 spatiotemporal data fusion by spectral correlation, which is more suitable for the regions where the spatial
158 information of objects has no obvious change, such as the Spatial and Temporal Adaptive Reflectance
159 Fusion Model (STARFM) and the improved STARFM (Gao et al., 2006; Hilker et al., 2009; Zhu et al.,
160 2010; Zhang et al., 2014). The other type of spatiotemporal data fusing method is data-driven, which
161 involves developing geostatistical models to solve the problem created when the same parameter is
162 inconsistent among different satellite products. This method includes the Kriging family of techniques
163 (Chatterjee et al., 2010; Li et al., 2014; Savelyeva et al., 2008), the spatiotemporal interpolation method
164 (Yang and Hu, 2018), and the Bayesian melding framework (Fuentes and Raftery, 2005; Christakos,
165 2010). However, these methods rely on Gaussian assumptions and linear models, which limits their
166 estimation accuracy (Nazelle et al., 2010; He and Kolovos, 2017). A nonlinear spatiotemporal
167 geostatistical method, Bayesian maximum entropy (BME), has been proposed to fuse the parameters that
168 have apparent spatiotemporal variations (Nazelle et al., 2010). The BME method can integrate
169 information from different sources and then consider the data uncertainties in achieving improved

170   prediction accuracy. The most important advantage of BME is that it does not restrict the complex
171   stochastic relationship between predictions/observations and 'true' values to the Gaussian linearized
172   model; this is an obvious breakthrough over approaches restricted to using normal distributions (Nazelle
173   et al., 2010; Li et al., 2013; Xu et al., 2019). The BME method has broad application in the assessment
174   of many different atmosphere parameters, such as ozone concentration (Nazelle et al., 2010; Bogaert et
175   al., 2009; Christakos et al., 2004), $PM_{2.5}$, PM_{10} (Yu and Wang, 2010; Beckerman et al., 2013), and aerosol
176   optical depth (Xia et al., 2022; Tang et al., 2016). These parameters have similar spatiotemporal
177   properties to CF, i.e., they vary rapidly in both time and space. Therefore, BME has the potential for use
178   in merging multiple satellite CF products to produce spatiotemporally complete, accurate, and coherent
179   Arctic CF products.

180   In this paper, we present a spatiotemporal data fusion framework based on a CDF matching
181   approach and BME methodology to generate a fused monthly CF product with 1°× 1° resolution in the
182   Arctic region from 2000 to 2020. The CDF matching approach is used to correct the bias of passive
183   sensor data based on active sensor data, thereby improving the quality of the passive data. The BME
184   method is used to produce spatiotemporally complete monthly CF data from corrected multiple-satellite
185   CF products. The uncertainties of passive sensor CF products benchmarked with active sensor data and
186   ground-based data are all considered in the fusing process. The study area was in the Arctic region above
187   60°N, including land and marine areas. The structure of this paper is as follows. Section 2 describes the
188   data, while Section 3 introduces the data preprocessing and methods. The results and discussion are
189   presented in Sections 4 and 5, respectively. Finally, the conclusions are provided in Section 6.

190   **2 Data**

191   **2.1 Satellite Data**

192   In view of the complementarity among the AVHRR-based, MODIS-based, and active sensor
193   products, this study involved ten passive-satellite-derived products from MODIS and AVHRR, with the
194   time period spanning from 2000 to 2020 along with an active-satellite-derived product from CALIPSO,
195   with the time period spanning from 2006 to 2016. The experimental period only included the sunlit
196   months from April to September because of the darkness of the Arctic winter. All the data are briefly
197   described in Table 1. Our study aimed to provide accurate and reliable measurements of cloud fraction
198   during the daytime in the Arctic region. To achieve this objective, we utilized cloud fraction data labeled
199   as "daytime" from multiple satellite datasets.

200   The AVHRR sensors are onboard sun-synchronous orbit satellites collecting data in the morning or
201   afternoon (NOAA, Metop-A/B). The morning (afternoon) orbits cross the equator on their descending
202   (ascending) node at approximately 0730 (1330) local time (LT). Starting with NOAA-17 and all MetOp
203   satellites, AVHRR data are available from a midmorning orbit with the equator crossing time at
204   approximately 0930 LT. However, complications arose from changes in the equatorial crossing times of
205   individual AVHRR sensors due to satellite drift (Heidinger et al., 2014; Karlsson et al., 2013). The
206   AVHRR has a nominal spatial resolution of 1.1 km at the nadir point, facilitating full global coverage
207   twice daily (daytime and nighttime), but the products this study employed provide global area coverage
208   data with a nadir footprint size of 1.1 km × 4.4 km (Stengel et al., 2017). Cloud detection algorithms of
209   these latest satellite data have improved greatly in polar regions. However, some data gaps exist as a
210   result of AVHRR scan motor errors (e.g., the NOAA-15 orbits were blacklisted in 2000 and 2001) and

limitations of observation conditions (e.g., CLARA-A2 could not cover the central Arctic Sea in September).

A MODIS sensor is onboard both the morning satellite Terra and the afternoon satellite Aqua, with overpass times at the equator of approximately 1030 LT and 1330 LT, respectively. The MODIS produces complete near-global coverage in less than 2 days. The 36 channels from the visible to thermal infrared spectrum provide abundant spectral information for cloud parameter retrieval. The new version datasets have improved the cloud detection algorithms in polar regions, whereas some researchers found overestimated CF in snow/ice surface in the new datasets when compared with active sensor data (Marchant et al., 2020; Marchant et al., 2016; Paul, 2017; Trepte et al., 2019). Although some differences exist between Terra and Aqua, the consistency between these two satellites cannot be ignored (Trepte et al., 2019).

The CALIPSO satellite combines an active light detection and ranging (lidar) instrument (Cloud-Aerosol Lidar with Orthogonal Polarization - CALIOP Lidar) with passive infrared (Imaging Infrared Radiometer) and visible imagers (Wide Field Camera) to probe the vertical structure and properties of thin clouds and aerosols worldwide (Winker et al., 2007; Vaughan et al., 2004; Hunt et al., 2009; Vaughan et al., 2009; Winker et al., 2009). As the most accurate currently active space-borne instrument for detecting clouds, CALIPSO has a 16-day repeat cycle with equatorial overpass time at 1:30 PM. The CAL_LID_L3_GEWEX_Cloud-Standard-V1-00 is a widely used grid cloud product with a spatial resolution of an equal angle grid 1°×1° (Claudia, 2012).

Table 1. Satellite cloud fraction products used in this research.

Products	Cloud detect method	Satellite	Sensor	Overpass time	Time range	Temporal resolution	Spatial resolution
MOD08-M3 Terra	MOD 35	Terra	MODIS	1030am	2000.2-2020.12	daily	1°x 1°
MYD08-M3 Aqua	MYD 35	Aqua	MODIS	1330pm	2002.7-2020.12	daily	1°x 1°
CERES-SSF Terra	CERES Edition 4	Terra	MODIS	1030am	2000.3-2020.12	daily	1°x 1°
CERES-SSF Aqua	CERES Edition 4	Aqua	MODIS	1330pm	2002.7-2020.12	daily	1°x 1°
CLARA-A2 AM	EUMETSAT NWC SAF PPS	NOAA-15	AVHRR3	0730am	2000.1-2000.7 2001.3-2002.7	daily	0.25°x 0.25°
		NOAA-17	AVHRR3	0930am	2002.8-2007.6		
		METOPA	AVHRR3	0930am	2007.7-2019.6		
CLARA-A2 PM	EUMETSAT NWC SAF PPS	NOAA-14	AVHRR2	1330pm	2000.1-2000.12	daily	0.25°x 0.25°
		NOAA-16	AVHRR3	1400pm	2001.1-2003.5 2003.6-2005.7		
		NOAA-18	AVHRR3	1330pm	2005.8-2009.5		
		NOAA-19	AVHRR3	1330pm	2009.6-2019.6		
PATMOS-x AM	Naive Bayesian	NOAA-15	AVHRR3	0730am	2000.1-2000.7 2001.3-2002.8	daily	0.1°x 0.1°
		NOAA-17	AVHRR3	0930am	2002.9-2007.6		
		METOPA	AVHRR3	0930am	2007.7-2020.12		
PATMOS-x PM	Naive Bayesian	NOAA-14	AVHRR2	1330pm	2000.1-2001.3	daily	0.1°x 0.1°
		NOAA-16	AVHRR3	1400pm	2001.4-2003.5 2003.6-2005.7		
		NOAA-18	AVHRR3	1330pm	2005.8-2009.5		
		NOAA-19	AVHRR3	1330pm	2009.6-2020.12		

ISCCP-H AM	IR and VIS threshold	NOAA-14-NOAA-19; METOPA	AVHRR2 / AVHRR3	9000am			
ISCCP-H PM				1500pm	2000.1-2017.6	daily	1°x 1°
CALIPSO-GEWEX	5km merged layer product level 2	CALIPSO	CALIOP	1330pm	2006.6-2016.12	Monthly	1°x 1°

2.2 Ground Observation Data

2.2.1 Climatic Research Unit Gridded Time Series

The Climatic Research Unit gridded Time Series (CRU TS) is a widely used climate dataset covering all land surfaces except Antarctica, which uses angular distance weighting to interpolate monthly climate anomalies from extensive networks of weather station observations onto a 0.5° grid (Harris et al., 2020; Harris et al., 2014). This dataset was first published in 2000, and the latest version, CRU TS4.05, contains ten variables including cloud cover for the period 1901–2020 (Harris et al., 2020). The percentage of cloud cover was derived from observations of sunlit hours, and CRU TS4.05 output files are actual values, not anomalies.

2.2.2 International Comprehensive Ocean-Atmosphere Data Set

The International Comprehensive Ocean-Atmosphere Data Set (ICOADS) is the most extensive freely available archive of global surface marine data, which has been assimilated into all major atmospheric, oceanic, and coupled reanalysis (Freeman et al., 2017). The ICOADS report is derived from synthetical observations of ships, buoys, coastal platforms, or oceanographic instruments. This dataset offers a gridded monthly summary for 2° latitude × 2° longitude boxes dating back to 1800 (and 1°×1° boxes since 1960) (Woodruff et al., 2005). The available climatic variables include cloud cover and other atmospheric parameters (Bojinski et al., 2014). In this study, we used the 1°×1° cloud cover data in sunlight months (April to September) spanning 2000 to 2020. In particular, we obtained the "fraction of observations in daylight" data from the ICOADS dataset, which allowed us to select only the data points corresponding to daytime observations. During our analysis, we imposed a threshold of 0.8 for the fraction of observations in daylight, ensuring that we only included the data with high confidence in our study.

2.3 Reanalysis Data and Model Data

In recent decades, atmospheric reanalysis datasets have emerged as a valuable resource for studying climate processes and predictability, offering a long-term, gridded depiction of atmospheric conditions. These datasets rely on state-of-the-art data assimilation systems, which integrate observational data and underlying models to create a continuous record of historical weather patterns. Through the use of various atmospheric variables, they provide insight into past weather phenomena. The utilization of these datasets could prove imperative in conducting research within areas that are limited in data availability, such as the Arctic. Several studies have investigated the performance of reanalyses over the Arctic for a variety of fields including CF (Yeo et al., 2022; Kennedy et al., 2012; Huang et al., 2017). However, the systematic errors of climatological reanalysis CF are substantial for Arctic clouds because of the complexity of cloud microphysical processes and lack of good observation. In-depth comparisons, as conducted by Walsh, have identified difficulties in adequately depicting persistent low-

265 level CF in summer via reanalysis models (Walsh et al., 2009).

266   ERA5 is an advanced atmospheric reanalysis product developed by the European Centre for
267 Medium-Range Weather Forecasts (ECMWF). It provides information on cloud properties, including
268 cloud fraction, cloud ice, cloud liquid, rain, and snow water content, which are estimated using the
269 prognostic equations developed by Tiedtke in 1993(Tiedtke, 1993). This method accounts for physical
270 processes that act as sources or sinks of clouds, such as convection and condensation. In addition, the
271 outdated diagnostic temperature-dependent approach for phase partitioning in mixed-phase clouds has
272 been replaced with a more sophisticated, prognostic method developed by Forbes and Ahlgrimm in
273 2014 (Forbes and Ahlgrimm, 2014). The updated radiation scheme in ERA5 employs the Monte Carlo
274 independent column approximation with generalized overlap for sub-grid cloud representation,
275 enhancing the accuracy of the product.

276   This study uses the CF of 'ERA5 hourly data on single levels from 1959 to present,' and the CF
277 parameter has been regridded to a regular lat-long grid of 0.25° and calculated by making assumptions
278 about the degree of overlap/randomness between clouds at different heights.

279   The climate model is also a valuable tool for climate studying. However, comparisons of climate
280 models to Arctic observations over the past three decades have revealed persistent challenges
281 simulating Arctic climate that partially attribute to imprecise cloud fraction (English et al. 2014). The
282 sixth phase Coupled Model Intercomparison Project (CMIP6) models have been used in many research
283 papers about climate. Among them the simulation data of the MRI-AGCM3-2-S climate model
284 provides a basis for climate research designed to answer fundamental scientific questions and serves as
285 a resource for authors of the Sixth Assessment Report of the Intergovernmental Panel on Climate
286 Change (IPCC-AR6). The model employed in this study is derived from the operational weather
287 prediction model of the Japan Meteorological Agency (JMA). It integrates quasiconservative semi-
288 Lagrangian dynamics, a radiation scheme, and a land surface scheme that was initially designed for a
289 climate model. Utilizing observed sea surface temperature (SST) as well as SST alterations forecasted
290 by atmosphere-ocean coupled models, we carried out simulations of both present-day and future
291 climate conditions. This model was released in 2017 and provided CF parameters at native nominal
292 resolutions of 25 km. This resolution employed in the model is as fine as that employed by regional
293 climate models (RCMs) in recent studies. Smallscale phenomena are realistically simulated in the high-
294 resolution model, with keeping the same quality of global-scale climate representation as the lower-
295 resolution models.

296   The study involved a comparison of pre- and post-fusion CF data with reanalysis and model data.
297 The aim was to underscore the significant role of fused data in improving the consistency of CF
298 between satellite observations, reanalysis data, and model data.

299 **3 Data Preprocessing and Methodology**

300   In this study, we propose a fusion algorithm framework that combines data from multiple satellites
301 to provide CF datasets with high spatiotemporal coverage and improved accuracy. Figure 1 shows a
302 flowchart of the general process, which includes four parts. First, the original data were preprocessed
303 before data fusion, a process that included data quality control and data resampling. Second, bias
304 correction of passive sensor data was conducted using active data with the CDF matching method. Third,
305 to comply with BME's stationarity prerequisite that assumes constancy of mean and variance, we
306 removed the spatiotemporal trend of the original satellite CF data over the study area using the

307 spatiotemporal moving window filter method. Fourth, the spatiotemporal covariance function was
308 modeled based on the isotropic residual data, and then the entropy was maximized with covariance
309 constraint. All the satellite-based CF data were treated as soft data so that the associated uncertainties
310 were incorporated into the fusing process.
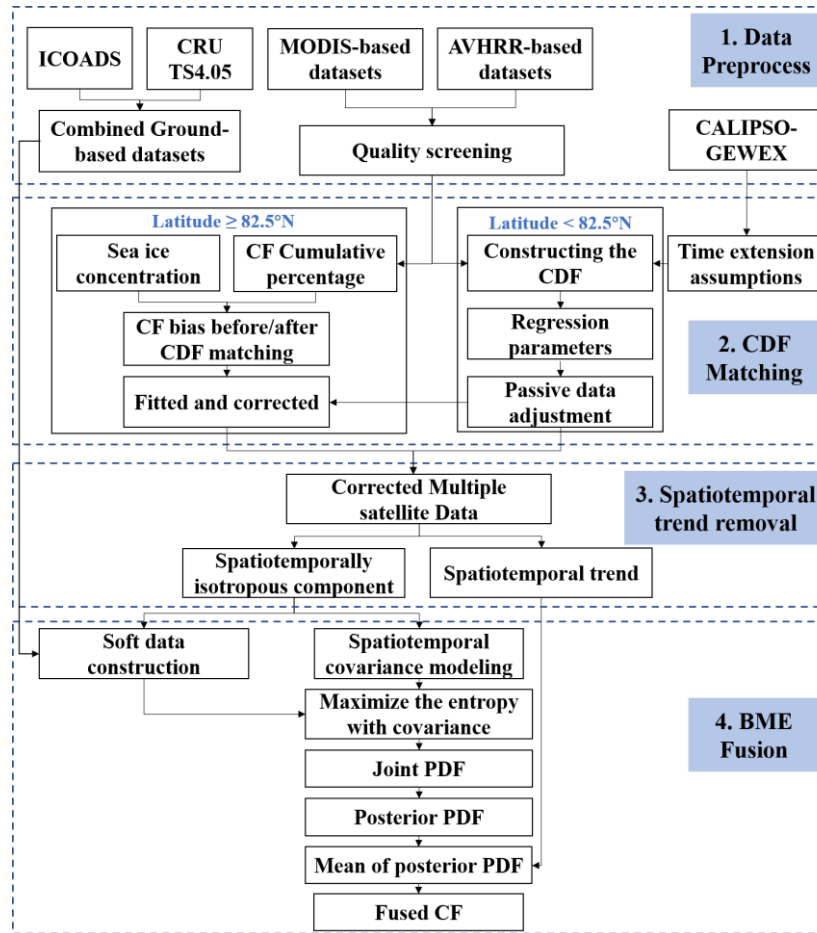
311

312 Figure 1. Flowchart for merging the multiple satellite cloud fraction products based on cumulative
313 distribution function matching and the Bayesian maximum entropy method.

314

3.1 Data Preprocessing

316   Over the Arctic, the cloud detection capabilities of passive sensors are always limited by spectral
317 channels, while active sensors are not susceptible to these effects (Liu et al., 2010; Liu et al., 2012b;
318 Kotarba, 2020; Shupe et al., 2013). To obtain more accurate fused CF results, it is necessary to correct
319 these passive sensor products using active sensor data before merging.

320   For satellite datasets, statistics always have the Scientific Data Set (SDS) name suffix
321 "_Standard_Deviation" and which are computed by calculating an unweighted standard deviation of all
322 pixels or samples within a given 1° grid cell. The large CF standard deviations (STDs) of satellite datasets
323 represent the large uncertainties of CF detection (Ackerman et al., 2008; Stengel et al., 2017). In this
324 study, we calculated the relationship between differences in STDs and CFs of passive/active sensor
325 datasets and found that the larger the standard deviation, the more serious the underestimation of passive
326 sensors. For the products with standard deviation flags, including MOD08 Terra/Aqua, CLARA-A2
327 AM/PM, and the PATMOS-x AM/PM, we used the 90 percentile of the daily standard deviation as scene-

328   based dynamic thresholds to screen CF data.

329   However, no standard deviation information was available for CERES-SSF Terra/Aqua and the

330   ISCCP-H AM/PM datasets. Based on research that shows ignoring optically very thin clouds could

331   increase the agreement between passive sensor data and the CALIPSO data, the 0.15 COT dataset was

332   selected as the quality threshold in this study.

333   **3.2 CDF Matching**

334   A widely used scaling strategy known as CDF matching can be used to adjust the distribution of the

335   target dataset to the range of reference data under the constant relative relationship. Several studies have

336   proved that the process of adjusting this distribution does not change the variation of original satellite-

337   based products, but rather aligns the value range with that of the reference data (Liu et al., 2011b; Brocca

338   et al., 2011; Xu and Cheng, 2021). Based on similar seasonal fluctuations of the passive sensor CFs and

339   active sensor data, the time series of passive sensor data from each grid box in the Arctic region were

340   adjusted to the values of the paired CALIPSO-GEWEX latitude and longitude grid. However, the

341   CALIPSO-GEWEX data could not cover regions with a latitude greater than 82.5°N and the temporal

342   range only covers 2006–2016. To correct the CF bias over the entire Arctic region, two strategies were

343   considered.

344   First, for the regions with enough reference data, the CF data of all passive sensors were directly

345   adjusted by CDF matching. The matching approach includes three steps: (1) constructing the cumulative

346   distribution function, (2) deriving regression parameters, and (3) adjusting the original data with

347   regression parameters. In our study, we use a three-month moving mean to eliminate the uncertainties in

348   CALIPSO-GEWEX data caused by the limitation of sampling quantities and frequencies. The filtered

349   daily passive sensor datasets were resampled as monthly mean data, and then the CDFs were constructed

350   for every dataset based on the same method used for the active data. A least-square fit was used to derive

351   the relationship between the reference and the target datasets. Based on the analysis of Liu et al.(2022),

352   the seasonal variation of CF for multiple satellites was greater than the interannual changes in CF (Liu

353   et al., 2022). We propose an additional assumption that the CDF ratio between active and passive sensor

354   data remains constant over the years in a 1°×1° grid cell.

355   Second, it was difficult to implement the CDF matching strategy for areas beyond the coverage of

356   active sensor data. Considering the relationship among the CF bias before and after CDF correction, the

357   cumulative percentage of CF (CPCF, the average CF over an interval of SIC), and the sea ice

358   concentration (SIC), a fitting function is proposed to correct the CF data.

359   After executing the abovementioned steps, we obtained the corrected multiple satellite data.

360   **3.3 Spatiotemporal Trend Analysis and Removal**

361   The BME theory was constructed based on the hypothesis of spatiotemporal random field (S/TRF)

362   (Nazelle et al., 2010; Christakos, 2000; He and Kolovos, 2017), which means that all the variables used

363   for this process are homogeneous and isotropous. However, a natural process that evolves in space–time,

364   such as the distribution of CF, can be divided into a heterogenetic global spatiotemporal trend and a

365   spatiotemporally isotropous residual, following Eq. (1):

$$CF_{(s,t)} = \overline{CF}_{(s,t)} + CF_{res(s,t)},$$

366   (1)

367   where (s, t) represents the space and time, $\overline{CF}_{(s,t)}$ represents the global spatiotemporal trend, and $CF_{res(S,t)}$

represents the stochastic anomalies of the variable. To meet the second-order stationarity assumption (constant mean and variance), it is necessary to remove the global spatiotemporal trend before estimating the spatiotemporally autocorrelated structure of the data (Spadavecchia and Williams, 2009; Tang et al., 2016). In this study, the global spatiotemporal trend was calculated using a spatiotemporal filter window with a size of 5° (longitude) × 5° (latitude) × 3 (months).

Figure 2 shows a histogram of the original combined satellite CF data, the global spatiotemporal trend, and the residual spatiotemporally isotropous component. From these distributions of the histogram, the residual is approximately normally distributed, which meets the requirement for modeling the structure of the spatiotemporal autocovariance.
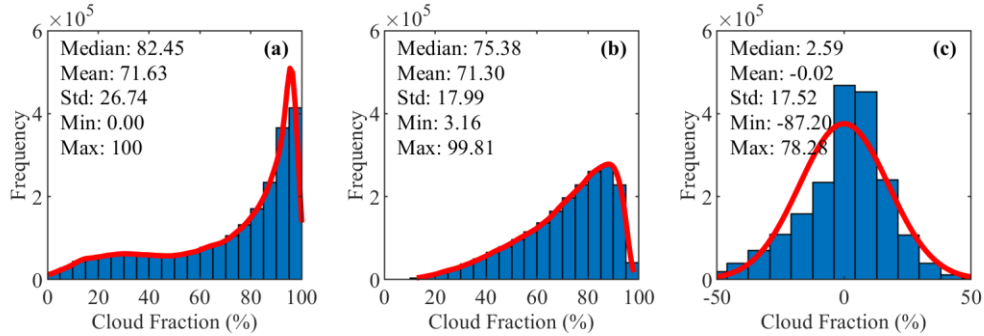
Figure 2. Histograms of (a) original combined satellite cloud fraction, (b) global spatiotemporal trend, and (c) spatiotemporally isotropous component, for the entire Arctic area (Example using 2010 data).

3.4 BME Fusion

3.4.1 Spatiotemporal Covariance Modelling

In spatiotemporal geostatistics, a covariance function indicates the spatial and temporal dependency of the data, which decreases as distance/time increases (Griffith, 1993). The spatiotemporal variation of the CF also can be expressed by a spatiotemporal covariance function. In the BME method, the experimental covariance can be calculated from the point pairs at specific distances and then modeled by the commonly used covariance model (Cressie, 2015). This study uses a nested covariance model with two spatiotemporal exponential models to model the spatiotemporal covariance of the detrended combined CF data, following Eq. (2):

$$\text{cov}(d,\tau) = c_1 \exp\left(-\frac{3d}{a_{s1}}\right)\exp\left(-\frac{3\tau}{a_{t1}}\right) + c_2 \exp\left(-\frac{3d}{a_{s2}}\right)\exp\left(-\frac{3\tau}{a_{t2}}\right), \qquad (2)$$

where d is the spatial lag and τ is the temporal lag between point pairs at coordinates $p(s, t)$ and coordinates $p'(s', t')$; c_1 and c_2 are the partial sill variances of the two exponential models; a_{s1} and a_{s2} are the spatial ranges of the two exponential models; a_{t1} and a_{t2} are the temporal ranges of the two exponential models. When the S/TRF is characterized by spatial and temporal stationarity, it is only the relative distance between any couple of locations that affects the covariance function. Specifically then, the covariance function has the same value $cx(p, p') = cx(r, t)$ for any location pair (p, p') separated by the same spatial distance vector r = s' - s and same temporal distance lag $\tau = t' - t$ (Christakos and Serre 2000). In this study, the parameters for spatiotemporal covariance are modeled separately for each year. The modelled results shown that the model has a spatial range of 2°, a temporal range of 3 months, and a partial sill variance of 0.85 for local scale CF (the first nested covariance model). And for the large range

401 CF the model has a spatial range of 30°, a temporal range of 6 months, and a partial sill variance of 0.15

402 (the second nested covariance model).

403

404 **3.4.2 Construction of Soft Data**

405 BME treated the informative content with uncertainty from different sources as soft data (He and

406 Kolovos, 2017). For example, the observed data that accompanied by obvious sources of uncertainty

407 such as inaccuracy in measuring devices, modeling uncertainties, and human error. In this study, the CF

408 data of passive sensor products are viewed as soft data. For the BME method, a key conceptual aspect is

409 that the framework does not impose any restrictive assumptions about the PDFs of soft data. Hence, a

410 parameterized statistical distribution of different sources of information can be used to replace the real

411 PDFs (Nazelle et al., 2010). Soft data could be probabilistic or interval soft data (Christakos, 2000). In

412 this study, the differences between satellite data and ground observations followed normal distributions

413 approximately. Therefore, the passive sensor data used for fusion were all treated as soft data with a

414 Gaussian distribution, following Eq. (3):

$$CF_{sate,x} = CF_{ground,x} + \varepsilon_x, \tag{3}$$

416 where $CF_{sate,x}$ and $CF_{ground,x}$ are the satellite CF data and the corresponding ground observation,

417 respectively, and ε_x is an independent random error, following Eq. (4):

$$\varepsilon \sim N\left(\mu_\varepsilon, \sigma_\varepsilon^2\right), \tag{4}$$

419 where μ_ε represents the mean of random error and σ_ε^2 represents the variance (Tang et al., 2016).
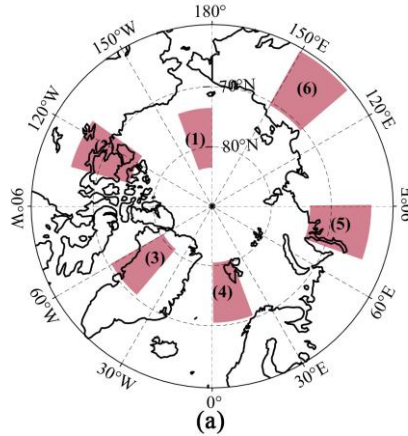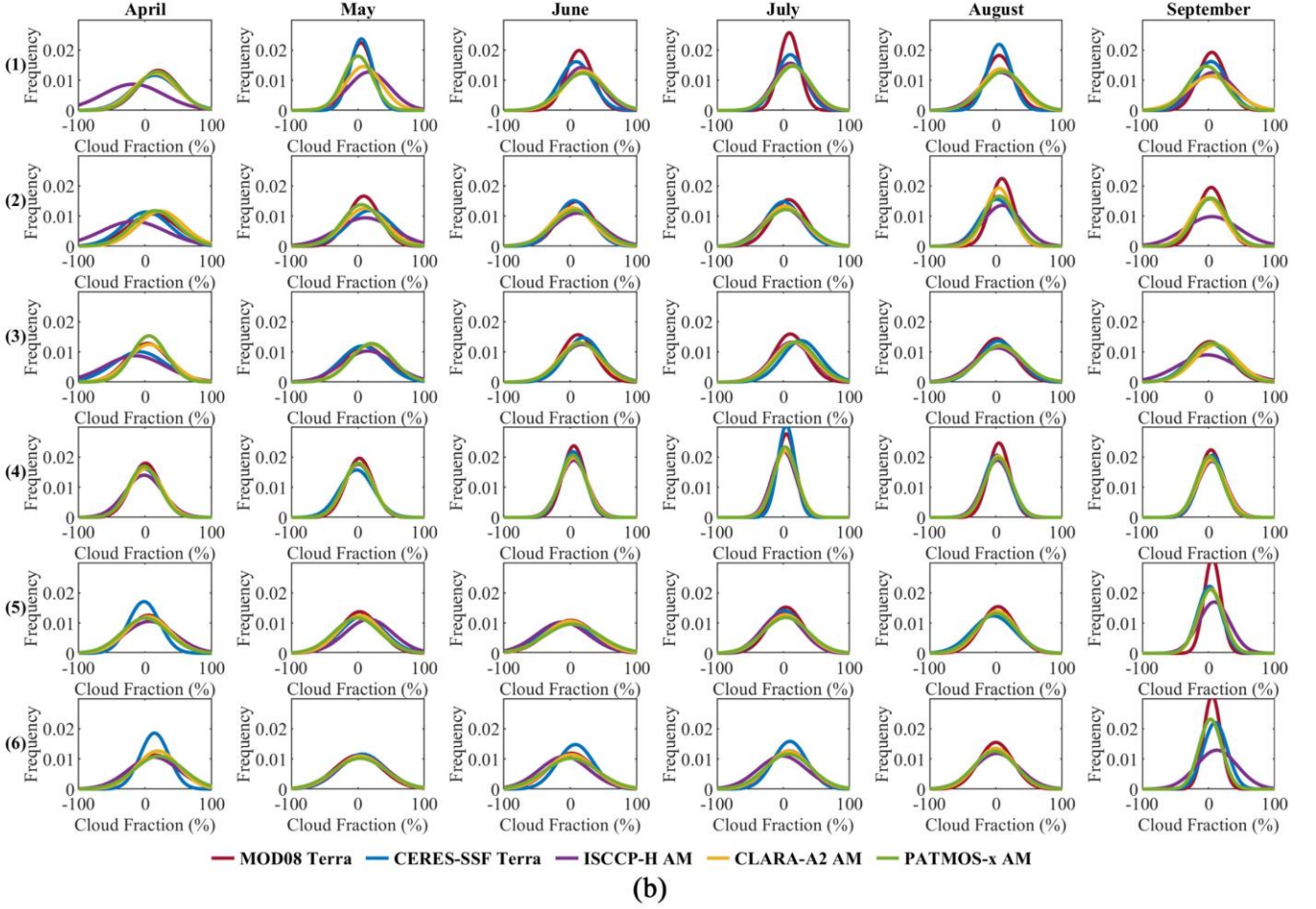
Figure 3. Gaussian probability density functions of the random errors between each type of satellite data and ground observations at six randomly selected regions of interest from April to September.

Because the uncertainties in each satellite CF data vary at different spatial and temporal scales, using the average uncertainty of the entire dataset to construct soft data over the entire study area will undoubtedly neglect the spatiotemporal variation of uncertainties. In this study, six regions were randomly selected to analyze the probability density functions (PDF) of random errors (Fig. 3). Large inconsistencies were observed for the PDF in land and ocean regions, and the temporal variation was also an important factor in inconsistencies. We constructed the soft data for CF data over land and ocean regions in every month separately. Considering the large errors in the Greenland Ice Sheet (GrIS), we calculated the PDF of random error separately for that region.

For each grid box, the CFs of different satellite data were converted into a Gaussian distribution probability soft data, individually (Tang et al., 2016). The soft data were expressed as:

$$CF_{soft,sate} \sim N\left(CF_{sate} + \mu_\varepsilon, \sigma_\varepsilon^2\right),$$
(5)

where CF_{sate} is the detrended CF value of multiple satellite datasets; the mean and variance of the Gaussian distribution probability soft data were expressed by $CF_{sate}+\mu_\varepsilon$ and σ_ε^2, respectively.

3.4.3 Using the BME Method for Multiple CF Data Fusion

The BME method can be used to merge continuous variables of satellite data for some atmospheric

438   parameters. To simplify the heterogeneity and anisotropic variability, the residuals were considered only

439   in the fusion process. Assuming that various adjacent observations from satellites were available with

440   irregular spatial and temporal gaps, the nonlinear mean estimation $\overline{x_k}$ of CF at the location (s_x, s_y) at

441   time t was estimated as:

$$\overline{x_k} = \int x_k f\left(x_k \mid x_{soft,1}, x_{soft,2} \ldots x_{soft,n}\right) dx_k, \tag{6}$$

443   where $f(x_k \mid x_{soft,1}, x_{soft,2} \ldots x_{soft,n})$ is a posterior PDF over the spatiotemporal adjacent grid observations, and

444   $x_{soft,1}, x_{soft,2} \ldots x_{soft,n}$ are the probabilistic Gaussian soft data derived from multiple satellite data. The

445   posterior PDF at the estimation point updates from the prior PDF in the Bayesian rule when soft data are

446   involved, so the relationship can be expressed as:

$$f\left(x_k \mid x_{soft,1}, x_{soft,2} \ldots x_{soft,n}\right) = \frac{f\left(x_{soft,1}, x_{soft,2} \ldots x_{soft,n}, x_k\right)}{f\left(x_{soft,1}, x_{soft,2} \ldots x_{soft,n}\right)}, \tag{7}$$

448   where $f(x_{soft,1}, x_{soft,2} \ldots x_{soft,n})$ represents the prior PDF of the spatiotemporally isotropous CF at the adjacent

449   grid, $f(x_{soft,1}, x_{soft,2} \ldots x_{soft,n}, x_k)$ is the joint PDF without specific information. Generally, the joint PDF is

450   represented by $f_g(x_{map})$, which can be calculated by maximizing the entropy under the constraint of the

451   general knowledge g (Jaynes, 1957). When predicting the probability distribution of a random event, the

452   larger the information entropy, the larger the amount of information obtained, and the result is closer to

453   the actual situation under a most uniform probability distribution. In this study, general knowledge is the

454   spatiotemporal covariance model, and to maximize the entropy, we introduce a Lagrange multiplier λ

455   (Xia et al., 2022).

$$f_g\left(x_{map}\right) = \frac{\exp\left(\sum_{\alpha=1}^{n} \lambda_\alpha g_\alpha\left(x_{map}\right)\right)}{\int \exp\left(\sum_{\alpha=1}^{n} \lambda_\alpha g_\alpha\left(x_{map}\right)\right) dx_{map}}, \tag{8}$$

457   Finally, the expectation of spatiotemporally CF isotropous component can be calculated by solving

458   these equations. Then the anisotropic spatiotemporal trend component of each grid was added to the

459   expectation at the corresponding point to obtain the merged CF product.

460   **4 Results**

461   **4.1 Result of CDF Matching**

462   Figure 4 shows the scatter plots of the CF distribution before and after CDF matching from multiple

463   passive and active sensors at the valid grid boxes with a latitude of less than 82.5°N. Based on the fact

464   that the assumption that the correction coefficient does not vary over time, the training datasets (T) were

465   processed from 2008 to 2014 and the validation datasets (V) were processed in 2006, 2007, 2015, and

466   2016. In Fig. 4, the 'Original CF (T)' and 'Original CF (V)' indicate the comparison of CALIPSO-

467   GEWEX CF and that of the original passive sensor data, so that the 'CDF CF (T)' and 'CDF CF (V)'

468   represent the comparison between CALIPSO-GEWEX CF and the corrected CF. In general, for all the

469   passive sensor datasets, the CFs after CDF matching were closer to the 1:1 line than before CDF matching.

470   R^2 increased by about 0.07–0.15, while that for ISCCP-H products was over 0.45. The RMSEs decreased

471   to one-third to one-half of what they were, and the biases decreased to approximately zero, which means

472   that the CDF matching obviously corrected outliers and eliminated the average differences between the

passive and active sensor CFs. From these scatter plots, we also understand that CDF matching plays an important role in low CFs (less than 60%), which was always seen in April or on the GrIS(Liu et al., 2022).

476
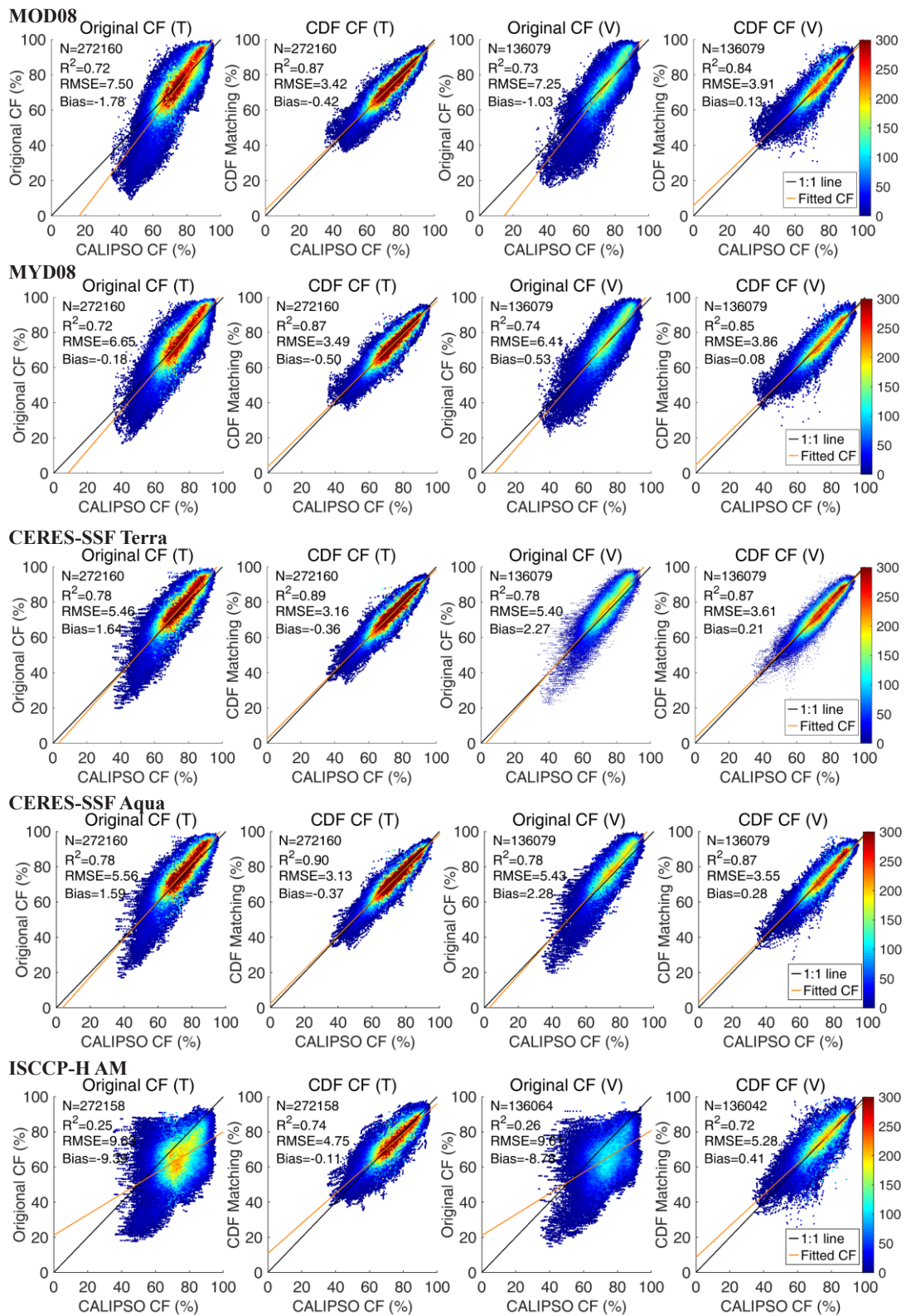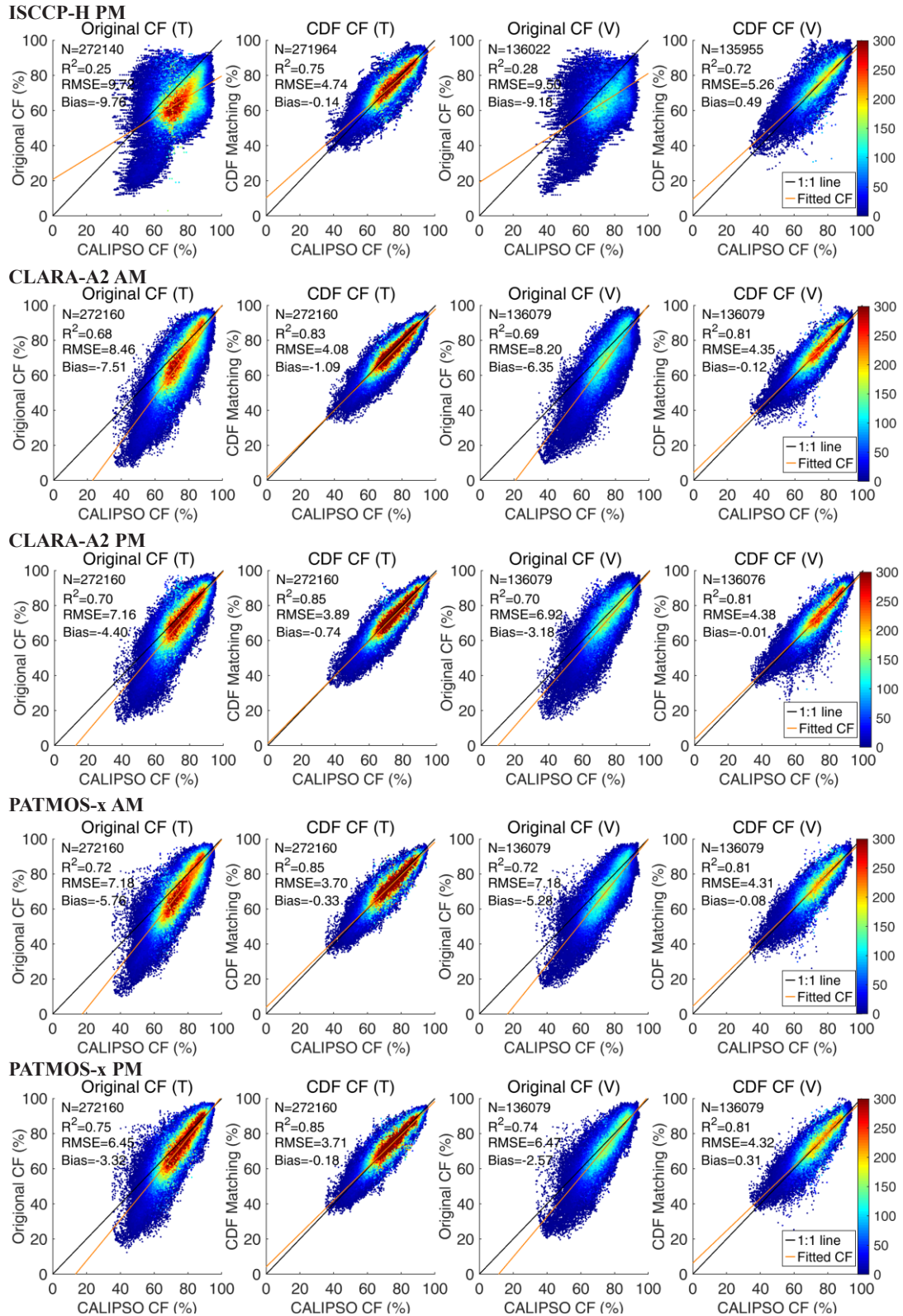
Figure 4. The scatter plots of the cloud fraction comparison between the passive and active sensor datasets at regions with latitudes less than 82.5°N before and after cumulative distribution function matching: (T) means training data with time ranges from 2008 to 2014 and (V) means validation data from 2006, 2007, 2015, and 2016.

480

In the sea ice regions, the relationships between CF bias of passive sensor data after and before CDF

482 matching, CPCF, and SIC are shown in Fig. 5. The results indicated that the mean of bias increased with

483 the SIC. Moreover, the CPCF appeared to decrease with increasing SIC, a negative correlation between

484 CPCF and bias was also evident.
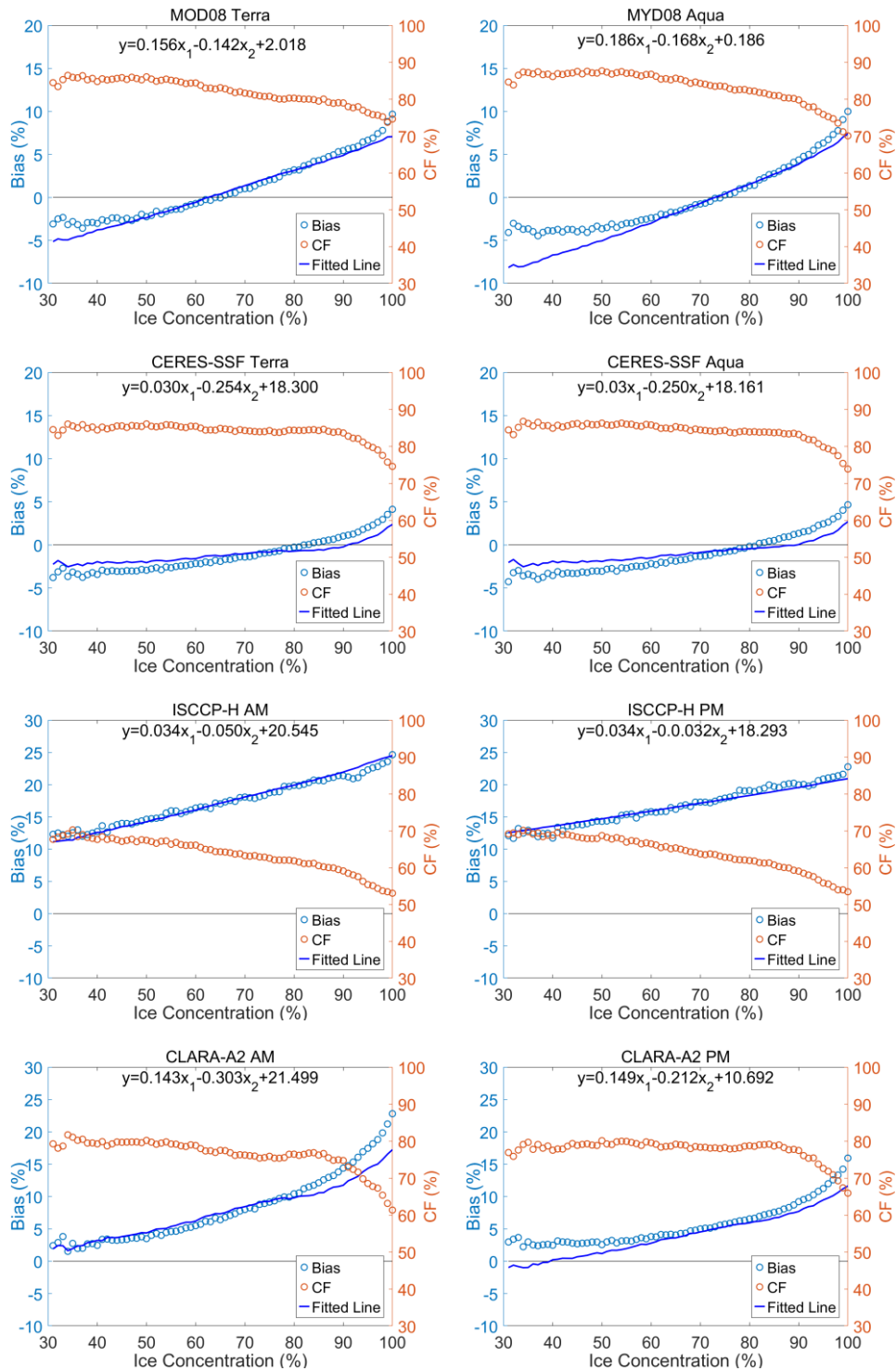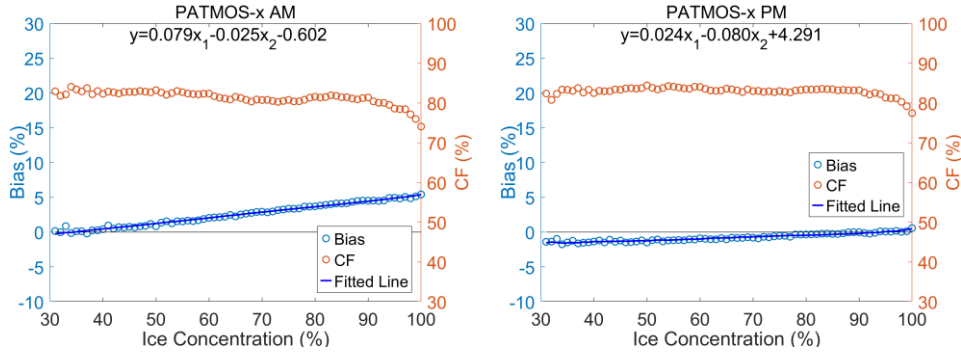
Figure 5. The relationship between cloud fraction bias of passive sensor data after and before cumulative distribution function matching, the cumulative percentage of cloud fraction, and the sea ice concentration in sea ice regions with latitude less than 82.5°N.

By virtue of this association, SIC and CPCF are modeled as dependent variables of the bias. Due to the predominant presence of sea ice over the domain located above 82.5N, we employ this functional association to remediate CF inaccuracies in the region, called C-SIC Corrected CF. Figure 6's initial two panels depict a comparison between the CF of active data and passive data before and after correction by C-SIC in sea ice regions below 82.5°N. The results indicate that R^2 of the corrected scatter plots increased slightly, but the RMSEs and bias were greatly reduced. In particular, the CF underestimated by passive sensors was similar to that of active sensors after correction. In our previous study, we have proven that this type of underestimation is very common(Liu et al., 2022). The third panel of Figure 6 shows the comparison of C-SIC Corrected CF and the CDF matching CF in sea ice regions with latitude less than 82.5°N. The results also showed that the C-SIC Corrected CFs have high degree of consistency with the CFs corrected by the CDF matching, with R^2 over 0.75, RMSE less than 3.6, and bias less than 0.5. However, although the correction has improved the ISCCP-H CFs, they also showed large inconsistencies with the passive sensor data and the CDF matching data. Therefore, the ISCCP-H CFs in regions north of 82.5°N were not included in the following fusion process.
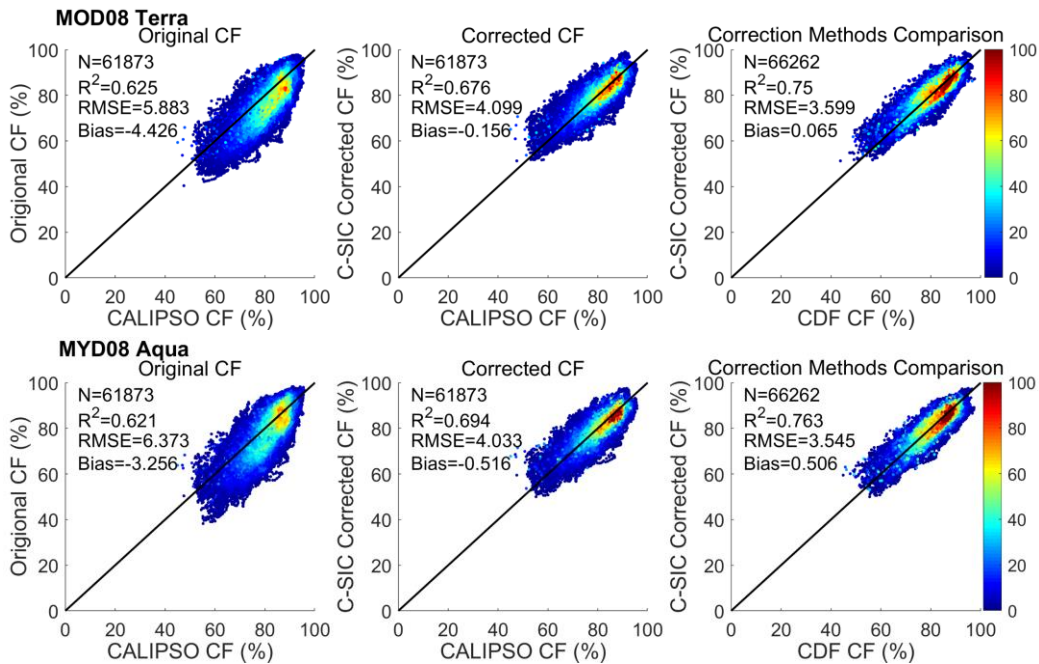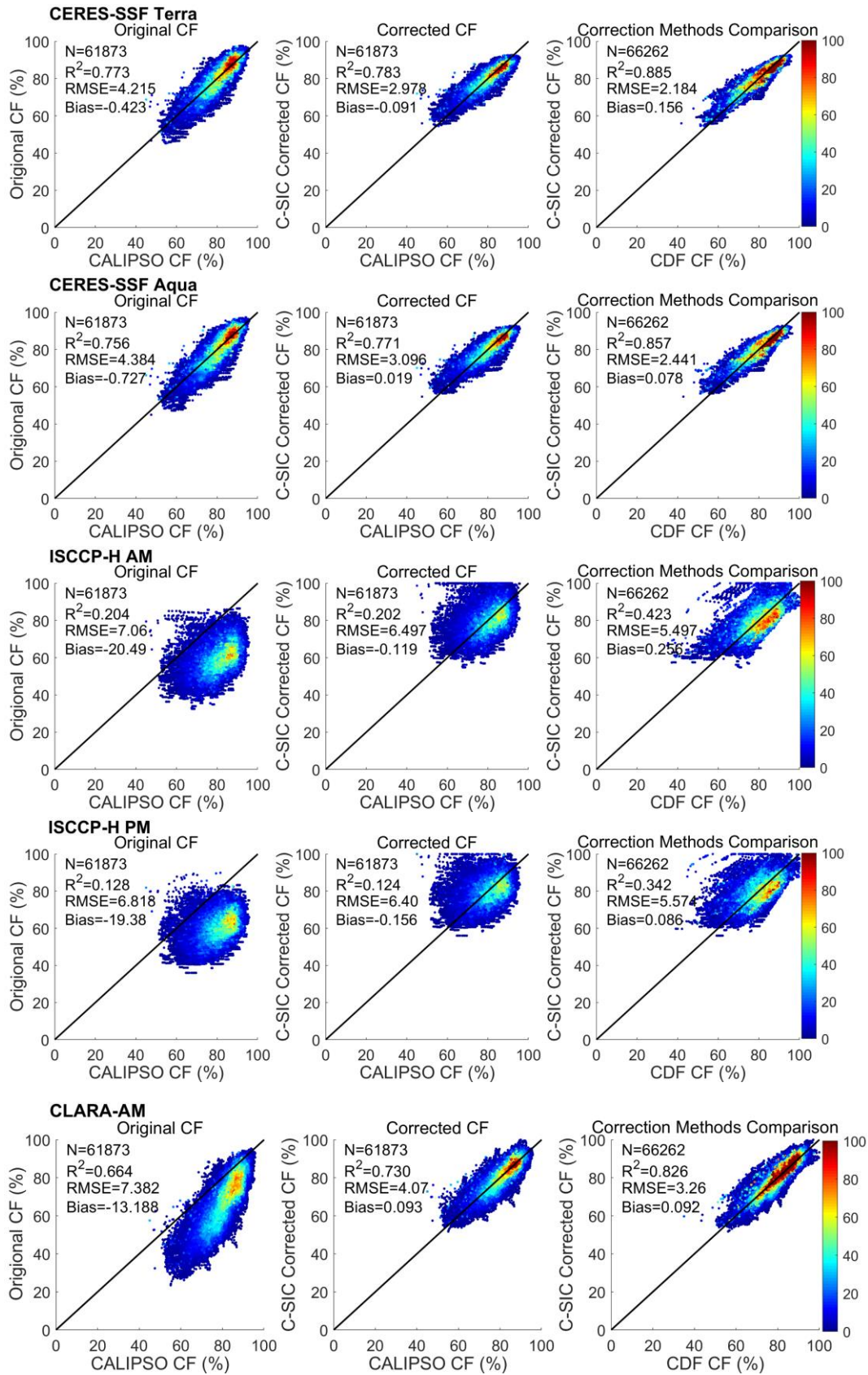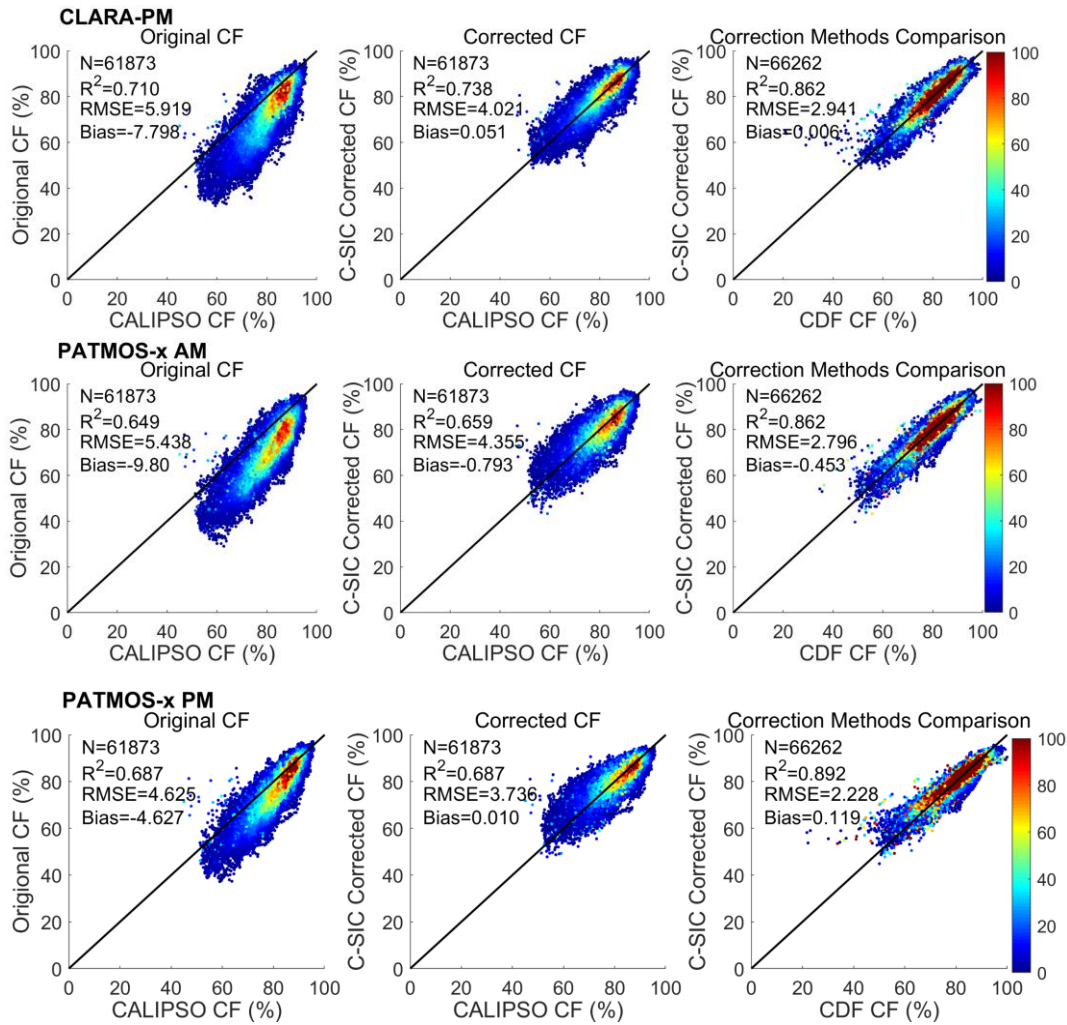
Figure 6. The scatter plots of the cloud fraction (CF) comparison between the passive sensor datasets and the active sensor dataset before (the first panel) and after (the second panel) using the method of CF corrected by the cumulative percentage of CF and SIC (C-SIC). And the scatter plots of the results comparison between C-SIC and cumulative distribution function matching (the third panel).

Accompanying the decreases in the CF differences of the active and passive sensor data, the accuracy of individual passive sensor datasets for the entire Arctic during the experimental period was also generally improved. Moreover, the consistency of multiple satellite data has improved greatly. Figure 7 displays the standard deviation between 1° × 1° passive sensor CF data before and after the application of cumulative distribution function matching (latitude≤82.5°N) and C-SIC correction (latitude >82.5°N). The results obtained from different regions indicate an obvious decrease in the inconsistency between multiple passive sensor data after the correction with the aforementioned methods. In the Holarctic region, multiple passive sensor CFs saw a decrease in mean STD from 9.18% to 5.75%, with more than 50% of the corrected data displaying a standard deviation within 5%. The sea ice region saw the largest reduction rate of the mean STD, approximately 4.5%. This reduction was mainly derived from a STD value range of 10–15%, due to the limited detection capacity of passive sensor data in sea ice areas. Regions with latitude less than 82.5°N saw a decrease in mean STD of only 3.02%. In contrast to the sea ice region, these land regions saw a smaller standard deviation between multiple satellite data. The distribution of STD frequency in regions over 82.5°N and the entire sea ice area appeared similar,

522 indicating that the C-SIC correction method was highly effective in 82.5°N regions. Although the relative

523 values showed improvement, the absolute change appeared inconspicuous.
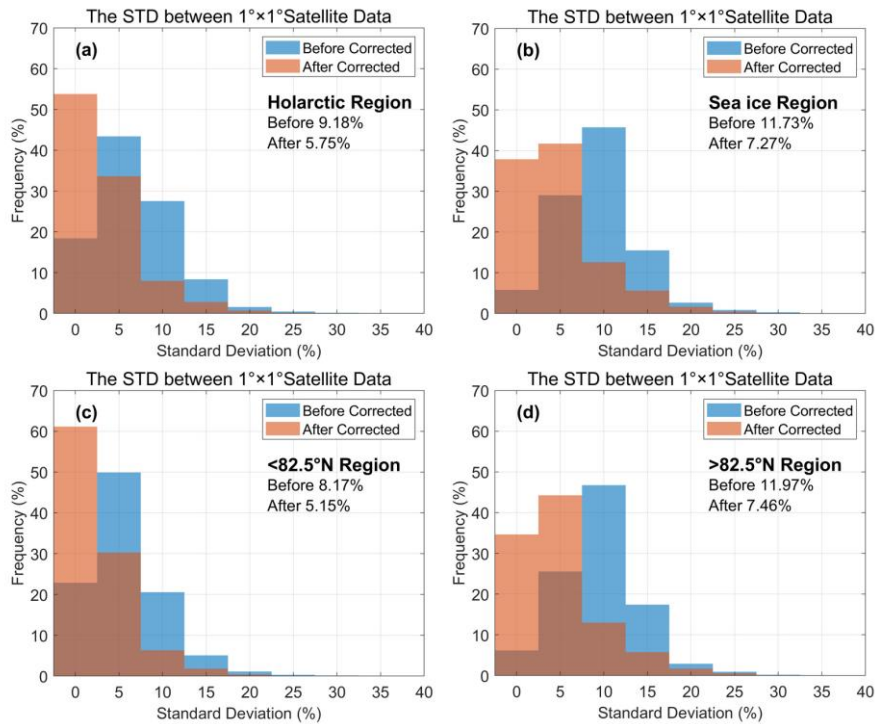
524

525 Figure 7. Standard deviation between 1° × 1° passive sensor cloud fraction before and after cumulative distribution

526 function matching (latitude<82.5°N) and C-SIC Corrected (latitude >82.5°N).

527

528 **4.2 Result of BME Fusing**

529 **4.2.1 Spatial and Temporal Distribution of the Fused CF**

530 Figure 8 shows the spatial distribution of Arctic CF from the fused product, multiple satellite data,

531 and ground observations. The results indicate that although most satellite-based products agreed

532 relatively well with the ground-based observations in both the geographical distribution and the zonal

533 average of Arctic CF at first glance, large disparities also appeared in some specific regions, whereas the

534 fused product we proposed reduced these disparities apparently. For instance, nearly all the passive and

535 active sensor products show the CFs over the GrIS were less than 60%. However, CFs of ground-based

536 observations over this region were reported as nearly 70%, which is closer to that of the fused product.

537 The sea regions of the central Arctic, which are covered by perennial sea ice/snow, are another area where

538 the passive sensor products always underestimate CF. From these figures, some passive sensor products,

539 especially for the AVHRR-based datasets, have CFs that are about 10–20% lower than those of active

540 sensor data and ground-based observations. However, the fused CF has a similar magnitude to these two

541 referred datasets.
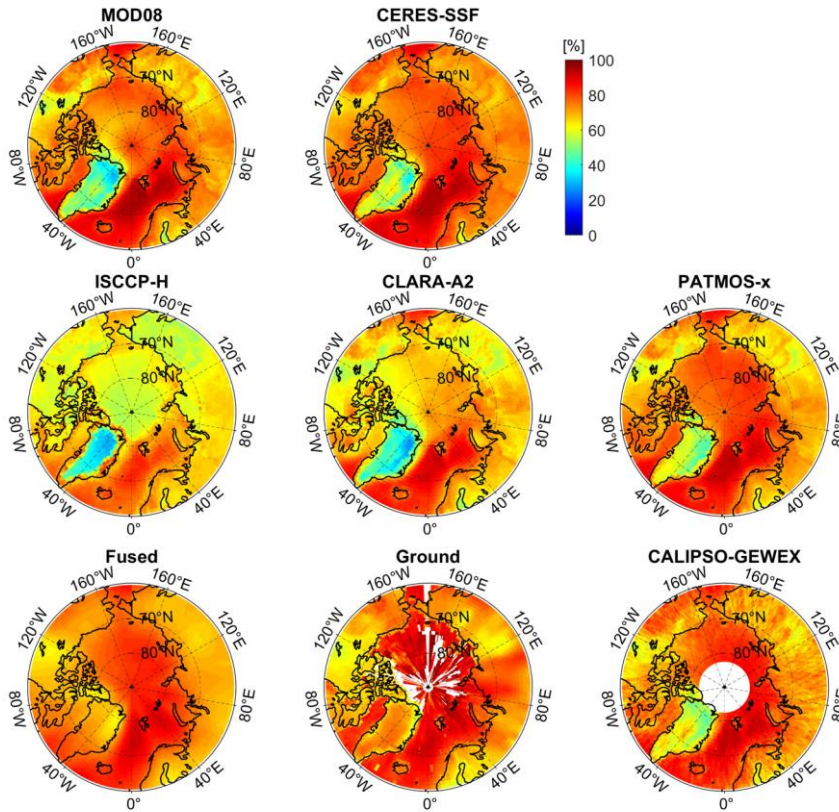
542

543  Figure 8. Distribution of the average cloud fraction of different datasets over the Arctic from 2000 to 2020. The

544  time ranges for ISCCP-H and CALIPSO-GEWEX were from 2000 to 2017 and from 2006 to 2016, respectively.

545

546  By contrast, the ground-based CF products have a large data gap because ground weather stations

547 are sparsely distributed in the Arctic, so the limitation of sampling quantities and frequencies had the

548 effect of limiting the spatial and temporal ranges of active sensor data. Moreover, the AVHRR-based

549 products often suffer from missing data as a result of satellite failures or band switching (Hollmann,

550 2018); in addition, some passive sensor products such as CLARA-A2 have some spatial gaps over the

551 Arctic Sea during autumn (Karlsson et al., 2017). Although we have eliminated a large number of low-

552 precision daily data in preprocessing, the completeness of the merged multiple-satellite CF products is

553 obviously higher than those of the original satellite-based data and ground-based observations in both

554 spatiality and temporality, especially in regions of the Arctic Ocean. The spatial completeness (the ratio

555 of available data to the CF grids of the entire Arctic) of the fused CF product was nearly 100%, which is

556 much larger than 54.09% of ground-based products and 73.15% of the active sensor product. Therefore,

557 the fusion algorithm proposed by this study can not only obviously reduce the inconsistencies of Arctic

558 CF between multiple satellite products and reference datasets but also effectively compensate for the data

559 gaps caused by the lack of reference data.

560  It is well known that the CF in the Arctic regions fluctuates apparently with the change in seasons.

561 To show the temporal accuracy of the fusion products, we analyzed the long time series area-weighted

562 mean of the CF. Figure 9 depicts the fluctuation of the mean value on a monthly basis for all data

563 during sunshine periods (April to September) before and after fusion, as demonstrated by the time

564 series. It is clear that the CF peaks in September and reaches a minimum in April. However, only the

565 fused product always maintains a high level of consistency with the reference data, with the monthly

mean CF varying from 62% to 79%. The overall area-weighted mean of the differences between fused CF and CALIPSO-GEWEX CF and between fused CF and ground-based CF was about 0.91% and 0.40%, respectively, which are about one-third of the differences for MODIS-based products and reference products and about one-fifth to one-twentieth of the differences for AVHRR-based products and reference products. In land and ocean areas, the fusion algorithm clearly corrects the outliers with large deviations, such as the CF from CLARA-A2, PATMOS-x products, and the CERES-SSF products. The first two datasets are well-known for underestimating the Arctic CF dramatically (Karlsson et al., 2017; Karlsson and Dybbroe, 2010). In this study, the underestimation mainly occurred in April, with approximately 8% and 3% for those two datasets, respectively. The latter has often been reported to overestimate CF (Doelling et al., 2016; Trepte et al., 2019), and in this study the CERES-SSF products nearly overmeasure CF all year long from April to September. However, the fusion framework proposed by this study scales these underestimated values or overestimated values to a range similar to that of active sensor data by CDF matching; meanwhile, it takes into account the deviation from ground observations in the BME fusion process. The fused CFs can not only reduce the overestimation of CF by MODIS-based products but also decrease the underestimation of CF for AVHRR-based products, which obviously improves the consistency of CF between the active sensor, passive sensor, and ground observation dataset compared with the original data.

Figure 9. The area-weighted means of cloud fraction over (a) Holarctic, (b) Land, and (c) Sea for different products in the Arctic from April to September during 2000 to 2020. The time ranges for ISCCP-H and CALIPSO-GEWEX were from 2000 to 2017 and from 2006 to 2016, respectively.

4.2.2 Quantitative Assessment of Fused CF

To validate the fused CF and compare the accuracy of the fused results to that of several original satellite CFs, all the passive sensor CF products and the merged CF product were spatiotemporally compared with the CRU TS4.05 in land regions and ICOADS measurements in sea regions. The correlation coefficient (R^2), root-mean-square error (RMSE), and mean bias (bias) were used to quantitatively evaluate the accuracies of the original and merged CF products. As Fig. 10 indicates, the scatters of the fused CF product and ground-based observations were closer to the 1:1 line than that of the original satellite data. In this case, the fused data had the largest R^2 (0.51), lowest RMSE (6.95%),

595 and the lowest bias (0.35%) for land regions. In addition, the fused data had the largest R^2 (0.42), the
596 lowest RMSE (5.62%), and the lowest bias (0.55%) for sea regions.

597
598 Figure 10. Validation of the fused cloud fraction and the original passive sensor datasets against the (a) CRU
599 TS4.05 and (b) ICOADS datasets.
600

601 For land, it can be also seen that the fusion results have a strong ability to correct the satellite CF
602 that is less than 30%. These values were mainly found on the GrIS, in the Canadian Islands, and on the
603 central Eurasian continent. In addition, the RMSE of CF after fusion was only one-half of the original
604 satellite data, which means that the overall distribution of the fused CF is better fitted to the reference
605 data, and most of the CFs with differences over 30% were well-corrected.
606 The observations of ICOADS come from multiple observation platforms, and most of these
607 platforms operate in open waters. The open water regions varied mostly with the growth and decline of
608 the SIC, which brings great spatiotemporal heterogeneity for the sampling of ICOADS. Therefore, in the
609 verification process, the first step was to spatiotemporally collocate the satellite data with ocean site.
610 Figure10 (b) shows that R^2 of the fused CF only improved by about 0.05–0.08 when compared with most
611 satellite data. However, the fusion algorithm reduces the RMSEs and bias obviously. The RMSEs of the
612 fusion CF were about one-fourth to one-third of the original MODIS-based products and one-third to
613 three-fifths of the original AVHRR-based products. The reductions of bias were about 4–5% for MODIS-

614   based products and about 2–5.4% for AVHRR-based products.
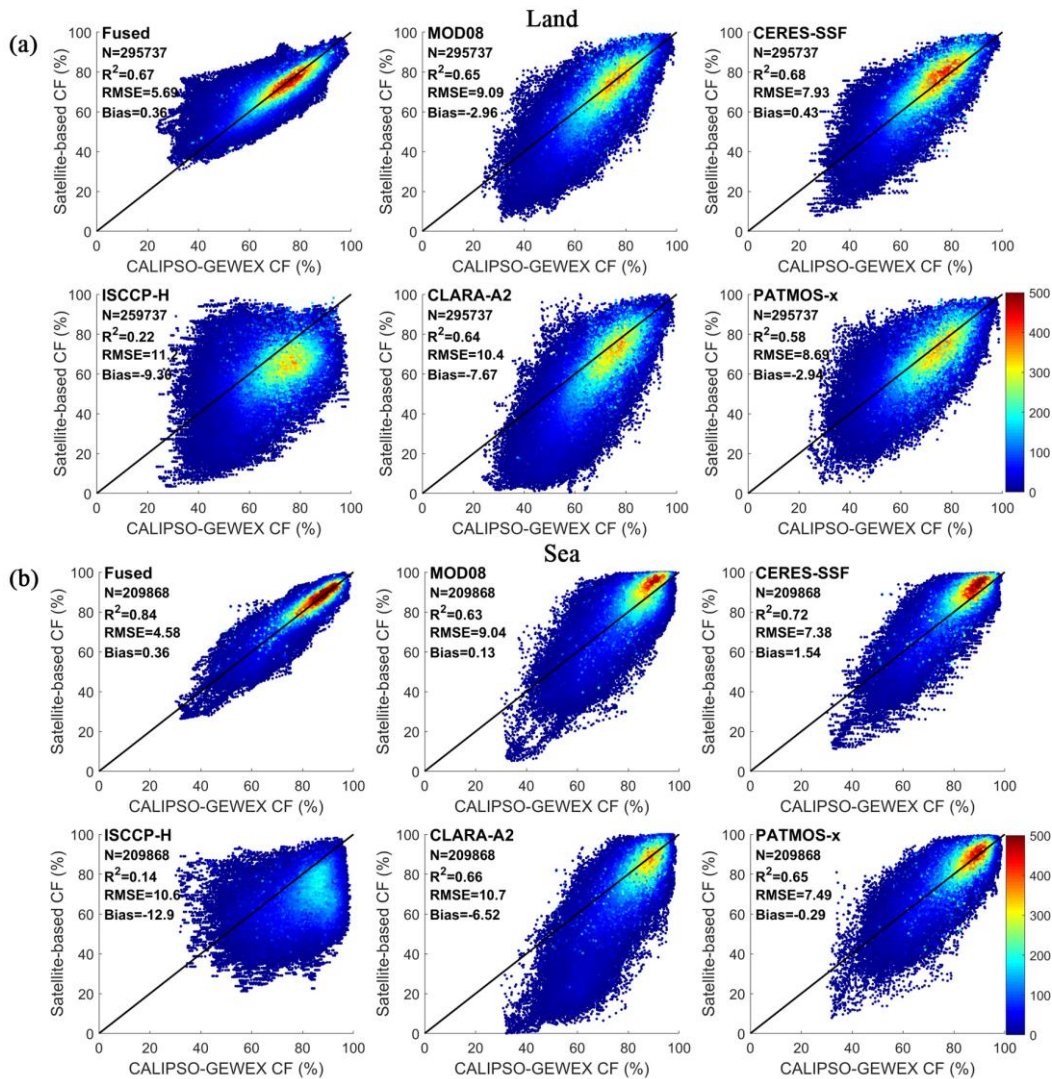
615
616   Figure 11. Validation of the fused cloud fraction and the original passive sensor datasets against the CALIPSO-
617   GEWEX dataset over (a) land and (b) sea regions, with a temporal range from 2006 to 2016.
618

619   As the accepted reference for passive sensor products, CALIPSO-based products are
620   considered to provide excellent data and are always used to validate the accuracy of cloud datasets.
621   In Fig. 11, we compare the CFs of passive sensor products before and after fusion with that of the
622   CALIPSO-GEWEX product. The results show that when compared with the original satellite data,
623   the consistencies between the fused product and the active sensor product were further improved in
624   both land and sea regions. The RMSEs were reduced to about one-third to one-half of the original
625   values, or approximately 5.69% and 4.58% for land and sea regions, respectively. Actually, the
626   consistency of CFs between passive and active sensor datasets was higher than that between satellite
627   data and ground observations. Except for the ISCCP-H products, R^2 of original satellite data was
628   over 0.63; that of fused CF only improved obviously in sea regions (about 0.12–0.21), while it
629   improved slightly but in inconspicuously in land regions (about −0.01–0.1). This can be explained
630   by the fact that the fusion algorithm greatly improves the low-value CFs in the land areas (especially
631   on the GrIS) to levels similar to that of ground-based observations, while the CF of the active sensor
632   data was no more than 60%. Therefore, some overestimations for the fused CF existed when

compared with the CALIPSO-GEWEX CF data. From the bias of Fig. 11 (a), we also see that the fusion algorithm can obviously improve the CF underestimated by the original satellite data. However, in the sea regions, the MODIS-based datasets seem to overidentify CF, especially when the CF was over 80%. Meanwhile, the AVHRR-based datasets show underestimation when CF was less than 80%. Obviously, the fused product corrected these CFs to a more suitable range.
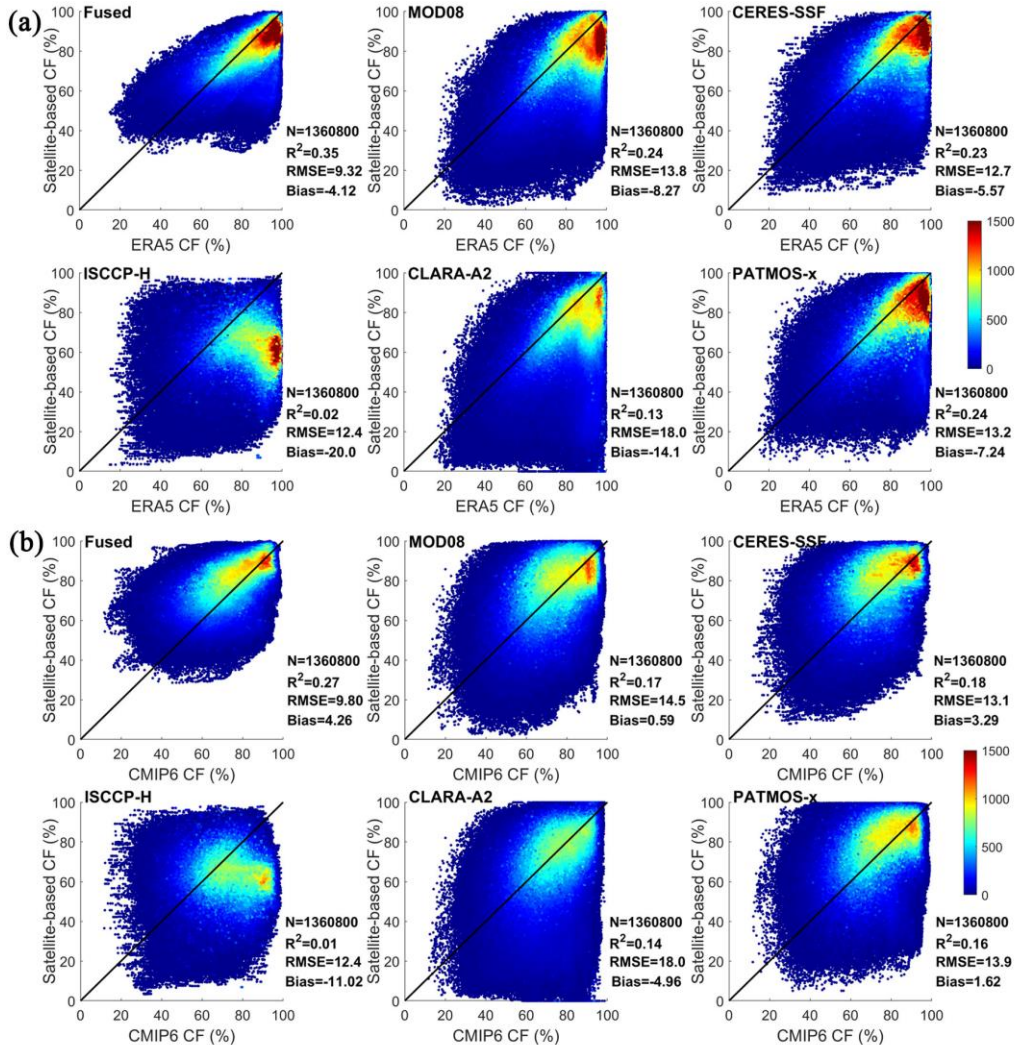
Figure 12. Validation of the fused cloud fraction (CF) and the original passive sensor datasets against (a) ERA5 CF dataset and (b) CMIP6 CF dataset over the Holarctic.

Reanalysis data and the climate model data are commonly used to provide a consistent and continuous dataset for long-term climate trends and variability studies. These datasets can provide insights into the behavior of the climate system that would be difficult to obtain from direct observations alone. To further show the advantages of the fusion results, we analyzed the difference in CFs between different satellite data, ERA5 reanalysis datasets and the MRI-AGCM3-2-S climate model. As can be seen from Fig. 12, the fusion product greatly reduced the deviation in CF between the satellite data and the reanalysis dataset and the model data. When compared with the ERA5 CF dataset, the scatters of fused CFs were more concentrated around the 1:1 line than those of the original satellite data. R^2 of the fusion product was about 1.5 times higher (improved about 0.18) than that of the original data, and the RMSEs and bias decreased to one-third of their original values (decreases of about 3.08–8.68% and 1.45–15.88%, respectively). This means that the distributions of the CFs over the entire Arctic of the fusion

product were more consistent with those of the reanalysis CF dataset than the original satellite. However, the low absolute values also indicated that there were inescapable inconsistencies in some grids. The ERA5 dataset has usually been reported to overestimate CF in some regions of the Arctic, especially in the ocean regions (Yeo et al., 2022). In these regions the fused CF has lightly higher values than that of the ERA5 data.

The comparison results with the MRI-AGCM3-2-S CF show that when compared with the original satellite data, the fusion method reduced the CF underestimation partly; these underestimations were often seen in April or over the central and western GrIS. In addition, R^2 was improved by about 0.14, and the RMSEs were reduced to one-fourth of their values of original satellite data (about 2.60–8.20% reduction). However, although the fusion data relieve some CF overestimations that occurred in original passive sensor datasets, the scatter plot in Fig. 12 shows that the fusion CFs in some grids were significantly higher than the CF of model data (with bias by 4.26%). These grids are usually found in the open water areas of Arctic Ocean, central Alaska, central Eurasia, and along the eastern margin of Greenland. Several studies have shown that the climate models underestimate the CF over these regions (Vignesh et al., 2020).

5 Discussion

5.1 The Efficacy of CDF Matching in CF Fusion

The CDF matching approach was operated based on a time series CF considering the time-varying process of CF products at a specific longitude–latitude grid box. Compared with the metrics for the traditional approach, the CF of multiple passive sensor products was scaled to a level similar to the active sensor CF after CDF matching, so that the inconsistencies among multiple passive sensor CF datasets were reduced. To further evaluate the efficacy of CDF matching in the CF fusion process, we quantitatively evaluated the deviation between satellite data before and after CDF correction with ground observation data.

By comparing Fig. 10 and Fig. 13, we can infer that CDF matching can obviously improve the low value of CFs typical of satellite data, making such data more similar to that observed by ground-based sites. These improvements were more obvious for CFs over land regions. Among them, the largest bias correction was seen for the ISCCP-H products (about 7.9% improvement) and the CLARA-A2 products (about 6.5% improvement); the former always underestimated CF in the Arctic (Kotarba, 2015; Liu et al., 2022) and the latter have often been reported to under-identify CF over northern Canada, northern Russia, and across the entire GrIS in land regions and over the entire Arctic Ocean in April (Karlsson and Dybbroe, 2010). Note that the bias of CERES-SSF changes from 0.4% to −0.72% after CDF matching, because CERES-SSF products are usually reported to overestimate CF and these overestimations were corrected reasonably. For the ocean regions, the ground references used in this paper were derived from multiple platform observations, which have great spatio-temporal heterogeneity. Therefore, a large CF discrepancy existed between satellite data and ocean observations. Almost all the passive sensor data have RMSEs and bias that would decrease after CDF correction by about 0.8–1.7% and 0.68–5.26%, respectively. The CDF matching mainly improves the CF in the high-value grid boxes of MODIS-based data and PATMOS-x data as well as in the CF in low-value grid boxes of ISCCP-H and CLARA-A2. Satellite observation covering open sea areas typically presents a higher CF compared to station observation. Consequently, partial overestimation may persist despite correction by the CDF

693   matching approach. In the subsequent fusion process, the difference between satellite CF and ground CF

694   was taken into account, which can play a certain extent role in overfitting correction.
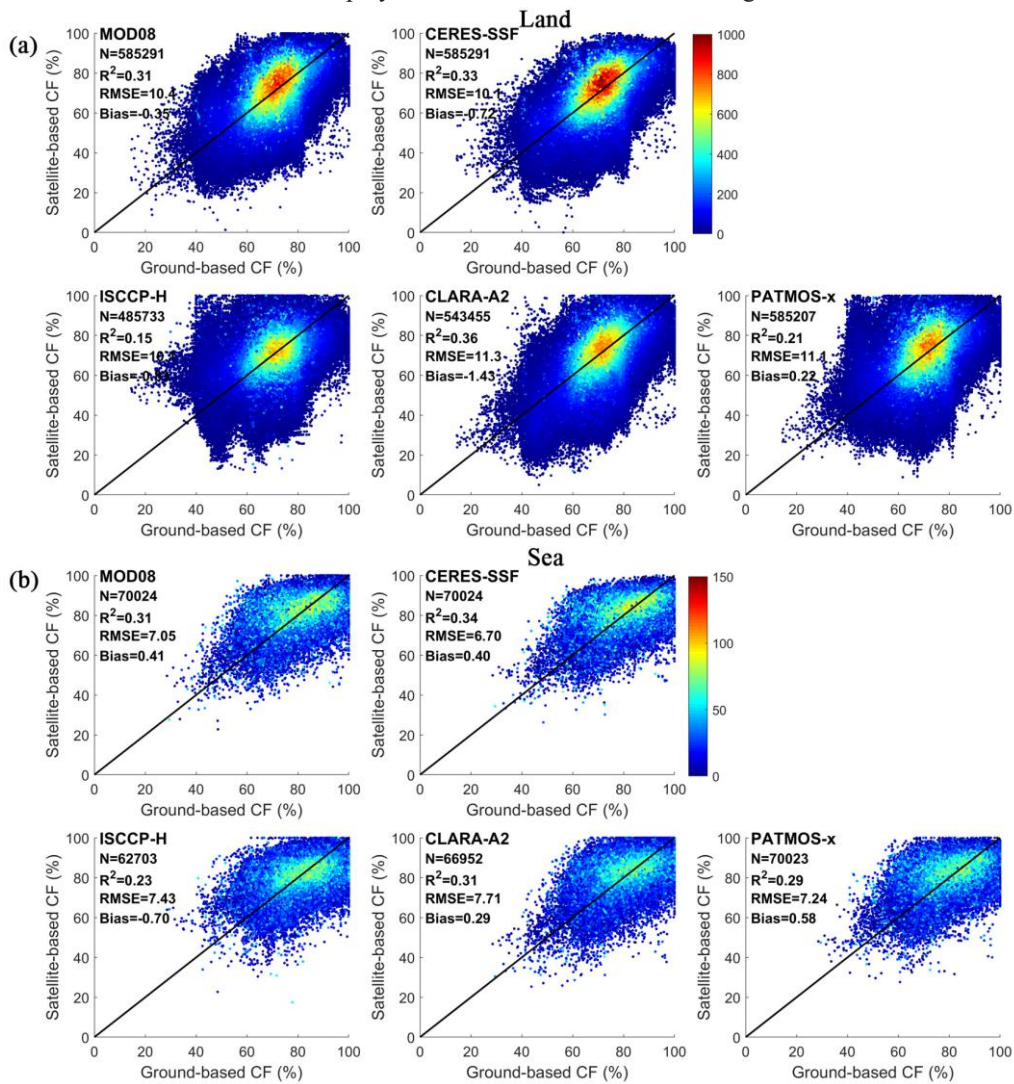
695
696   Figure 13. Validation of the corrected cloud fraction of passive sensor datasets after cumulative distribution

697   function matching against (a) CRU TS4.05 dataset over land regions and against (b) ICOADS dataset over sea

698   regions.

699

700   In addition, in the land area, CDF matching was directly carried out grid by grid. However, the short

701   temporal range (2006–2016) of the reference data limits the production of long time-series CF products.

702   In this study, we proposed a hypothesis that the matching parameter in a specific grid box does not change

703   over time. To prove the validity of this hypothesis, we conducted sensitivity analysis on the matching

704   parameters from the fifth to the eleventh year at one-year intervals. The findings indicate that any

705   deviations in matching parameters were under 0.05% when the time horizon exceeded 8 years. This

706   demonstrates a level of stability in the correction coefficient when utilizing data for a period exceeding

707   11 years (Figure A1). Figure 14 displays the variation in differences between satellite data and ground

708   observations before and after conducting CDF matching throughout the duration of the study. These

709   differences are calculated by subtracting the deviation between satellite data and ground observations

710   subsequent to CDF matching from that prior to CDF matching. Clearly, the differences remained steady

711   over time, and the maximum average annual difference was no more than 1.56%, while part of it was

712   derived from the orbit drift of satellite and variations in the spectral channel.
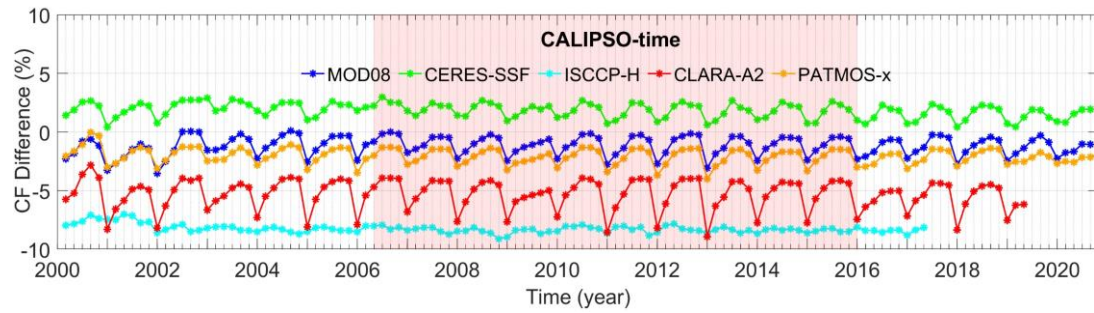
713
714   Figure 14. The difference in results between satellite data and ground observations before and after cumulative
715   distribution function matching over the Arctic from 2000 to 2020.
716

717   **5.2 The Uncertainties of the original Satellite Data**

718   CF products from different sensors have different degree of uncertainties. As a knowledge-centered
719   approach, Bayesian maximum entropy approach could integrate informative content with uncertainty
720   from different sources based on a rigorous theoretical support of considerable generality to achieve
721   improved prediction accuracy. For example, the observed data that accompanied by obvious sources of
722   uncertainty such as inaccuracy in measuring devices, modeling uncertainties, and human error are treated
723   as soft data in BME strategy. For the CF datasets of multiple satellite, the uncertainties come from
724   calibration error, orbit drift, signal degradation as well as the errors of cloud detection algorithms (Liu et
725   al., 2022). To achieve optimum estimation of CFs by combining data from multiple sensors, it is
726   imperative to explicitly consider the uncertainties associated with the CF data that is being merged. In
727   our study, the CF data of passive sensor products are viewed as soft data, and the uncertainty associated
728   with different error sources can be expressed explicitly by probability distribution.
729   Specifically, the soft data of multiple satellite CF datasets were constructed by comparing the
730   spatiotemporally collocated satellite CFs and the ground-based records from CRU TS4.05 over land and
731   from ICOADS over sea. Traditionally, the deviations between each satellite dataset and ground site
732   observations at different times and different regions have been averaged to the entire datasets, and then
733   used to calculate the average uncertainty of these data. In this way, the spatial variation of uncertainty in
734   each satellite dataset was ignored. Because the conditions that cause uncertainty are variable in time and
735   space, the uncertainties in each satellite dataset were definitely not the same everywhere (Tang et al.,
736   2016). This is especially true for the ICOADS data, which come from different platforms and introduce
737   large inconsistencies in results. In this study, we constructed soft data for CF over land, ocean, and GrIS
738   regions every month separately by analyzing the PDF differences for different regions and different
739   months, which realized more consistent results with the ground observations. However, despite concerted
740   efforts, determining the uncertainty for each grid remains challenging in light of the substantial temporal
741   and spatial gaps of the reference data, particularly that which pertains to the marine domain.

742   **5.3 The Uncertainties of the Fusion CF**

743   To assess the fusion algorithm's reliability, we used the standard deviation of error within each grid value
744   in the fusion process to quantify the uncertainties. Specifically, we determined the standard deviation of
745   the predicted posterior probability density function on each grid point. Our findings demonstrate that,

with the exception of the northern region of Greenland and part of the margin error, the standard deviation of error in other areas was within 3% (Fig 15). We attribute these discrepancies primarily to the underestimation of ground and satellite observations by satellite data, particularly ISCCP-H data, by around 10-30% in the central zone of Greenland. Moreover, the CF of ISCCP-H was significantly overestimated beyond the Greenland margin. Such significant inconsistencies can adversely affect the fusion results. In addition, because the CF of satellite data, particularly satellite data based on AVHRR, was significantly lower than that of ground observation data and active sensor data in April, and a significant difference existed between different datasets, the standard deviation of error after fusion marginally increased in April, with some areas at approximately 4%.
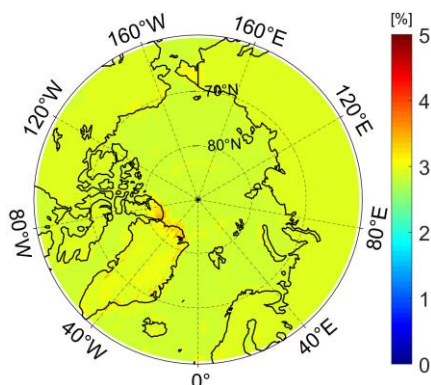
Figure 15. The mean error standard deviation of the fusion results

6 Data Availability

The fused CF product is available on the Zenodo repository at https://doi.org/ 10.5281/zenodo.7624605 (Liu et al., 2022). The gridded CF data are provided both in *.mat format (Fused_CF_Arctic_MAT, with file size 9.91 MB) and netCDF format (Fused_CF_Arctic_netCDF, with file size 10.7MB) at 1° spatial resolution and monthly temporal resolution during 2000–2020 in percentages. The results in these two folders are exactly the same, someone can download either format as needed.

7 Conclusions

The spatiotemporal inconsistency in existing satellite CF products would inhibit their application in climatological and energy budget studies. Over the Arctic region, the special climatic conditions and underlying surface characteristics limit the cloud detection abilities of passive/optical satellite sensors. The complementary features of the CF products derived from multiple satellite sensors in spatial completeness and accuracy make it possible to produce an improved CF product by merging data from multi-sensor satellite CF products.

In this paper, we propose a data fusion strategy for producing high-quality monthly CF data over the entire Arctic with a latitude larger than 60°N during sunlit months from 2000 to 2020. Four key steps were involved in the proposed strategy: (1) data quality control; (2) correct the bias of passive sensor data using CDF matching; (3) obtain the spatiotemporally isotropous component by removing the spatiotemporal trends; and (4) produce very accurate CF data by fusing multiple satellite products and considering the uncertainty between satellite data and ground observations with the BME approach.

The fusion algorithm proposed by this study apparently reduced inconsistencies in the Arctic CF data acquired by multiple satellite products and the reference products spatiotemporally, resulting in 10–20% reductions of CF differences between fused satellite products and the reference data, and an obvious improvement was seen across the GrIS and in the central Arctic Ocean. The results from 21-year data sets in the study areas demonstrate that the monthly mean CF of the fusion product varied from 62% (April) to 79% (September) during the study period, which is similar to that of the two reference datasets. After CDF matching, the inconsistencies of multiple satellite CF products were reduced by about 3.43% for the entire Arctic, with a larger reduction (4.46%) for sea ice regions. The overestimation of MODIS-based products and the underestimation of AVHRR-based products have been effectively corrected, with the CERES-SSF bias changing from 0.4% to −0.72% and the bias of ISCCP-H and CLARA-A2 decreasing by about 7.9% and 6.5%, respectively. After BME fusing, comparisons with the ground-based observations (CRU TS4.05 in land and ICOADS in marine areas) and the active sensor data CALIPSO-GEWEX show that R^2 improved by about 0.05–0.48 for different products; meanwhile, the overall RMSEs and bias of fusion product were reduced by about 2.08–7.75% and 1.6–12.54%, with reductions of nearly 50% and 67% when compared with that of the original passive sensor data, respectively. When compared with the reanalysis CF dataset ERA5 and the model dataset MRI-AGCM3-2-S, R^2 increased by about 0.18 and 0.14, RMSE and bias for reanalysis data decreased by about one-third of that for the original data, with reductions about 3.08–8.68% and 1.45–15.88% for different data, respectively. The RMSEs for model data dropped to one-fourth of their original values (about a 2.60–8.20% reduction). These mean that the proposed fusion algorithm effectively removed CF data with differences greater than 30% and made the fused Arctic CF estimation more robust than those data from a single satellite. Nevertheless, the fused product could completely cover the entire Arctic, especially the ocean regions, where the active sensor data and the ground-based data have large data gaps. Temporally, the fused data can complement the missing data caused by the faults of satellites carrying AVHRR sensors and the absence of Aqua data before 2002 as well as the temporal limitation of passive sensors.

In general, the proposed fusion algorithm combines the complementary features of multiple satellite CF datasets; it not only takes full advantage of the spatiotemporal autocorrelation among neighboring grids but also incorporates uncertainty estimates of multi-sensor CFs, such as the uncertainties of each passive sensor dataset, the uncertainties between passive and active sensor datasets, as well as the uncertainties between satellite data and ground-based observations. Through temporal and spatial expansion schemes, this fusion framework makes up for the disadvantages in spatiotemporal ranges of reference data. Finally, the fusion algorithm can generate monthly $1° × 1°$ CF product covering the entire Arctic region during 2000 to 2020, which has positive significance for reducing the uncertainties of assessment of surface radiation flux and improving the accuracy of research related to climate change and energy budgets both regionally and globally. However, some overestimations were observed, especially in ocean regions. This may be attributed to the fact that the ocean stations are too sparse to play a certain role in correcting the overfitting of CDF. Although ICOADS is a widely used ocean validation dataset, it has great spatiotemporal heterogeneity because it comes from a variety of different observation platforms and the sampling is affected by the extent of sea ice. Better reference data should be explored to further improve the uncertainty involved in the assessment of the fused product.

 Appendix A

818
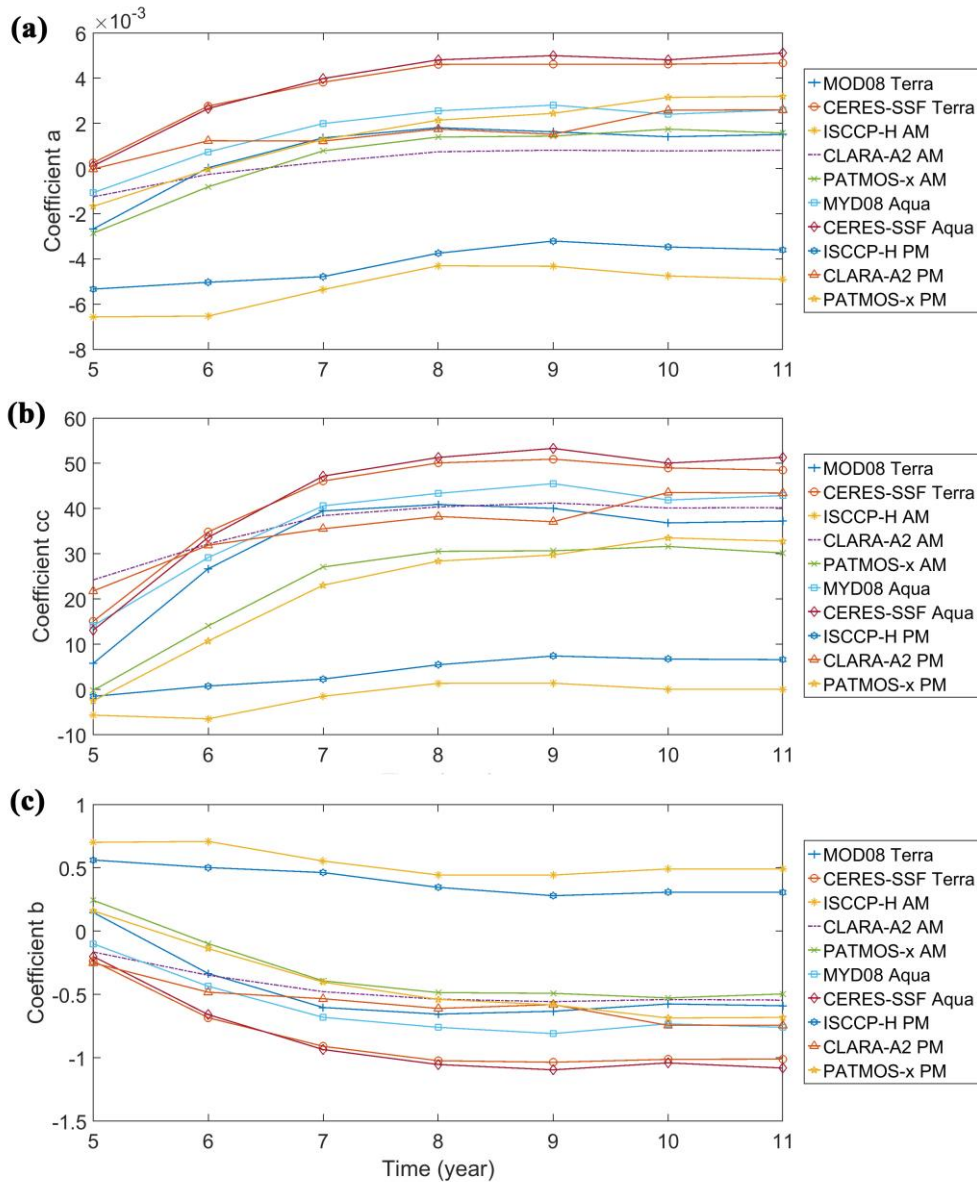
Figure A1. The sensitivity analysis on the CDF matching parameters from the fifth (2011) to the eleventh year (2017) of CALIPSO time at one-year intervals. The Coefficient a, b and c are calculated by the least-square fit method. And the time period only contains sunlight month from April to September.

Author contributions

XL performed the method, validation, and writing the original draft of the paper. TH was responsible for conceptualization, supported and supervised the study and reviewed the paper. SL was responsible for conceptualization and reviewed the paper. RL provided guidance on data processing. XX, RM and YM contributed to the editing and revising of the manuscript. XL prepared the manuscript with contributions from all co-authors.

828   **Competing interests**

829   The contact author has declared that none of the authors has any competing interests.

830   **Disclaimer**

831   Publisher's note: Copernicus Publications remains neutral with regard to jurisdictional claims in
832   published maps and institutional affiliations.

833   **Acknowledgments**

834   We thank the relevant teams and organizations for providing the data sets used in this study. We
835   thank the NASA Level-1 and Atmosphere Archive & Distribution System Distributed Active Archive
836   Center (LAADS DAAC) for providing the MOD08_M3/MYD08_M3 products, the NASA Langley
837   Research Center Atmospheric Science Data Center (ASDC) for providing CERES_SSF and CALIPSO-
838   GEWEX data, the Satellite Application Facility on Climate Monitoring (CM SAF) for providing the
839   CLARA-A2 product, the NOAA National Centers for Environmental Information (NCEI) for providing
840   PATMOS-x and ISCCP-H products. We also thank the University of East Anglia Climatic Research
841   Unit for their providing the CRU TS4.05 data, the NOAA Physical Sciences Laboratory for their
842   providing the ICOADS marine data, and the European Centre for Medium-Range Weather Forecasts
843   (ECMWF) for their archiving the ERA5 data. Many thanks to the LetPub (http://letpub.com.cn/) for its
844   linguistic assistance during the preparation of this manuscript.

845   **Financial support**

846   This work was supported by the National Natural Science Foundation of China Grant (42090012).

847   **References**

848   Ackerman, S. A., Holz, R. E., Frey, R., Eloranta, E. W., Maddux, B. C., and McGill, M.: Cloud detection
849   with MODIS. Part II: Validation, Journal of Atmospheric and Oceanic Technology, 25, 1073-1086,
850   10.1175/2007jtecha1053.1, 2008.

851   Beckerman, B. S., Jerrett, M., Serre, M., Martin, R. V., Lee, S.-J., van Donkelaar, A., Ross, Z., Su, J., and
852   Burnett, R. T.: A Hybrid Approach to Estimating National Scale Spatiotemporal Variability of PM2.5 in
853   the Contiguous United States, Environmental Science & Technology, 47, 7233-7241, 10.1021/es400039u,
854   2013.

855   Bogaert, P., Christakos, G., Jerrett, M., and Yu, H. L.: Spatiotemporal modelling of ozone distribution in
856   the State of California, Atmospheric Environment, 43, 2471-2480, 10.1016/j.atmosenv.2009.01.049,
857   2009.

858   Bojinski, S., Verstraete, M., Peterson, T. C., Richter, C., Simmons, A., and Zemp, M.: THE CONCEPT
859   OF ESSENTIAL CLIMATE VARIABLES IN SUPPORT OF CLIMATE RESEARCH, APPLICATIONS,

860   AND POLICY, B Am Meteorol Soc, 95, 1431-1443, 10.1175/bams-d-13-00047.1, 2014.

861   Brocca, L., Hasenauer, S., Lacava, T., Melone, F., Moramarco, T., Wagner, W., Dorigo, W., Matgen, P.,
862   Martínez-Fernández, J., Llorens, P., Latron, J., Martin, C., and Bittelli, M.: Soil moisture estimation
863   through ASCAT and AMSR-E sensors: An intercomparison and validation study across Europe, Remote
864   Sensing of Environment, 115, 3390-3408, 10.1016/j.rse.2011.08.003, 2011.

865   Chatterjee, A., Michalak, A. M., Kahn, R. A., Paradise, S. R., Braverman, A. J., and Miller, C. E.: A
866   geostatistical data fusion technique for merging remote sensing and ground-based observations of aerosol
867   optical thickness, Journal of Geophysical Research-Atmospheres, 115, 10.1029/2009jd013765, 2010.

868   Christakos, G.: Modern Spatiotemporal Geostatistics, Modern spatiotemporal geostatistics2000.

869   Christakos, G.: Integrative problem-solving in a time of decadence, Springer Science & Business Media
870   2010.

871   Christakos, G., Kolovos, A., Serre, M. L., and Vukovich, F.: Total ozone mapping by integrating
872   databases from remote sensing instruments and empirical models, Ieee Transactions on Geoscience and
873   Remote Sensing, 42, 991-1008, 10.1109/Tgrs.2003.822751, 2004.

874   Christakos G, Serre ML.: BME analysis of spatiotemporal particulate matter distributions in North
875   Carolina. Atmospheric Environment 34:3393–3406,2000.

876   Claudia, S., William R., Stefan K.: Assessment of Global Cloud Data Sets from Satellites A Project of
877   the World Climate Research Programme Global Energy and Water Cycle Experiment (GEWEX)
878   Radiation Panel, World Climate Research Program Proport, 2012.

879   Cressie, N.: Statistics for spatial data, John Wiley & Sons2015.

880   Danso, D. K., Anquetin, S., Diedhiou, A., Kouadio, K., and Kobea, A. T.: Daytime low-level clouds in
881   West Africa - occurrence, associated drivers, and shortwave radiation attenuation, Earth Syst Dynam, 11,
882   1133-1152, 10.5194/esd-11-1133-2020, 2020.

883   Doelling, D. R., Sun, M., Nguyen, L. T., Nordeen, M. L., Haney, C. O., Keyes, D. F., and Mlynczak, P.
884   E.: Advances in Geostationary-Derived Longwave Fluxes for the CERES Synoptic (SYN1deg) Product,
885   Journal of Atmospheric and Oceanic Technology, 33, 503-521, 10.1175/Jtech-D-15-0147.1, 2016.

886   Drusch, M.: Observation operators for the direct assimilation of TRMM microwave imager retrieved soil
887   moisture, Geophysical Research Letters, 32, 10.1029/2005gl023623, 2005.

888   Eastman, R. and Warren, S. G.: Arctic Cloud Changes from Surface and Satellite Observations, Journal
889   of Climate, 23, 4233-4242, 10.1175/2010jcli3544.1, 2010.

890   Enriquez-Alonso, A., Sanchez-Lorenzo, A., Calbo, J., Gonzalez, J. A., and Norris, J. R.: Cloud cover
891   climatologies in the Mediterranean obtained from satellites, surface observations, reanalyses, and CMIP5
892   simulations: validation and future scenarios, Climate Dynamics, 47, 249-269, 10.1007/s00382-015-
893   2834-4, 2016.

894   Forbes, R. M. and Ahlgrimm, M.: On the Representation of High-Latitude Boundary Layer Mixed-Phase
895   Cloud in the ECMWF Global Model %J Monthly Weather Review, 142, 3425-3445,
896   https://doi.org/10.1175/MWR-D-13-00325.1, 2014.

897   Freeman, E., Woodruff, S. D., Worley, S. J., Lubker, S. J., Kent, E. C., Angel, W. E., Berry, D. I., Brohan,

P., Eastman, R., Gates, L., Gloeden, W., Ji, Z., Lawrimore, J., Rayner, N. A., Rosenhagen, G., and Smith, S. R.: ICOADS Release 3.0: a major update to the historical marine climate record, International Journal of Climatology, 37, 2211-2232, 10.1002/joc.4775, 2017.

Fuentes, M. and Raftery, A. E.: Model evaluation and spatial interpolation by Bayesian combination of observations with outputs from numerical models, Biometrics, 61, 36-45, 10.1111/j.0006-341X.2005.030821.x, 2005.

Gao, F., Masek, J., Schwaller, M., Hall, F. J. I. T. o. G., and sensing, R.: On the blending of the Landsat and MODIS surface reflectance: Predicting daily Landsat surface reflectance, 44, 2207-2218, 2006.

Griffith, D. A.: STATISTICS FOR SPATIAL DATA - CRESSIE,N, Geographical Analysis, 25, 271-275, 1993.

Hakuba, M. Z., Folini, D., Wild, M., Long, C. N., Schaepman-Strub, G., and Stephens, G. L.: Cloud effects on atmospheric solar absorption in light of most recent surface and satellite measurements, 10.1063/1.4975543, 2017.

Harris, I., Jones, P. D., Osborn, T. J., and Lister, D. H.: Updated high-resolution grids of monthly climatic observations - the CRU TS3.10 Dataset, International Journal of Climatology, 34, 623-642, 10.1002/joc.3711, 2014.

Harris, I., Osborn, T. J., Jones, P., and Lister, D.: Version 4 of the CRU TS monthly high-resolution gridded multivariate climate dataset, Sci Data, 7, 109, 10.1038/s41597-020-0453-3, 2020.

He, J. and Kolovos, A.: Bayesian maximum entropy approach and its applications: a review, Stochastic Environmental Research and Risk Assessment, 32, 859-877, 10.1007/s00477-017-1419-7, 2017.

Heidinger, A. K., Evan, A. T., Foster, M. J., and Walther, A.: A Naive Bayesian Cloud-Detection Scheme Derived from CALIPSO and Applied within PATMOS-x, Journal of Applied Meteorology and Climatology, 51, 1129-1144, 10.1175/Jamc-D-11-02.1, 2012.

Heidinger, A. K., Foster, M. J., Walther, A., and Zhao, X. P.: The Pathfinder Atmospheres-Extended Avhrr Climate Dataset, Bulletin of the American Meteorological Society, 95, 909-+, 10.1175/Bams-D-12-00246.1, 2014.

Hilker, T., Wulder, M. A., Coops, N. C., Linke, J., McDermid, G., Masek, J. G., Gao, F., and White, J. C.: A new data fusion model for high spatial- and temporal-resolution mapping of forest disturbance based on Landsat and MODIS, Remote Sensing of Environment, 113, 1613-1627, 10.1016/j.rse.2009.03.007, 2009.

Hollmann, R.: ESA Cloud_cci Product Validation and Intercomparison Report(PVIR), 10.5676/DWD/ESA_Cloud_cci/AVHRR-PM/V002, 2018.

Hollmann, R., Merchant, C. J., Saunders, R., Downy, C., Buchwitz, M., Cazenave, A., Chuvieco, E., Defourny, P., de Leeuw, G., Forsberg, R., Holzer-Popp, T., Paul, F., Sandven, S., Sathyendranath, S., van Roozendael, M., and Wagner, W.: THE ESA CLIMATE CHANGE INITIATIVE Satellite Data Records for Essential Climate Variables, B Am Meteorol Soc, 94, 1541-1552, 10.1175/bams-d-11-00254.1, 2013.

Hu, M. and Xue, M. J. G. r. l.: Implementation and evaluation of cloud analysis with WSR-88D reflectivity data for GSI and WRF-ARW, 34, 2007.

Huang, Y. Y., Dong, X. Q., Xi, B. K., Dolinar, E. K., Stanfield, R. E., and Qiu, S. Y.: Quantifying the

937 Uncertainties of Reanalyzed Arctic Cloud and Radiation Properties Using Satellite Surface Observations,

938 Journal of Climate, 30, 8007-8029, 10.1175/Jcli-D-16-0722.1, 2017.

939 Hunt, W. H., Winker, D. M., Vaughan, M. A., Powell, K. A., Lucker, P. L., and Weimer, C.: CALIPSO

940 Lidar Description and Performance Assessment, Journal of Atmospheric and Oceanic Technology, 26,

941 1214-1228, 10.1175/2009jtecha1223.1, 2009.

942 Jaynes, E. T. J. P. r.: Information theory and statistical mechanics, 106, 620, 1957.

943 Jin, W., Fu, R.-d., Ye, M., and Li, J.-x.: Meteorological Cloud Image Fusion Using Contourlet Transform

944 and Compressed Sensing, International Conference on Ecological Protection of Lakes-Wetlands-

945 Watershed and Application of 3S Technology (EPLWW3S 2011), Nanchang, PEOPLES R CHINA, 2011

946 Jun 25-26, WOS:000391516000097, 413-416, 2011.

947 Karlsson, K.-G., Anttila, K., Trentmann, J., Stengel, M., Meirink, J. F., Devasthale, A., Hanschmann, T.,

948 Kothe, S., Jaaskelainen, E., Sedlar, J., Benas, N., van Zadelhoff, G.-J., Schlundt, C., Stein, D.,

949 Finkensieper, S., Hakansson, N., and Hollmann, R.: CLARA-A2: the second edition of the CM SAF

950 cloud and radiation data record from 34 years of global AVHRR data, Atmospheric Chemistry and

951 Physics, 17, 5809-5828, 10.5194/acp-17-5809-2017, 2017.

952 Karlsson, K. G. and Devasthale, A.: Inter-Comparison and Evaluation of the Four Longest Satellite-

953 Derived Cloud Climate Data Records: CLARA-A2, ESA Cloud CCI V3, ISCCP-HGM, and PATMOS-

954 x, Remote Sens-Basel, 10, 10.3390/rs10101567, 2018.

955 Karlsson, K. G. and Dybbroe, A.: Evaluation of Arctic cloud products from the EUMETSAT Climate

956 Monitoring Satellite Application Facility based on CALIPSO-CALIOP observations, Atmospheric

957 Chemistry and Physics, 10, 1789-1807, DOI 10.5194/acp-10-1789-2010, 2010.

958 Karlsson, K. G. and Hakansson, N.: Characterization of AVHRR global cloud detection sensitivity based

959 on CALIPSO-CALIOP cloud optical thickness information: demonstration of results based on the CM

960 SAF CLARA-A2 climate data record, Atmos Meas Tech, 11, 633-649, 10.5194/amt-11-633-2018, 2018.

961 Karlsson, K. G., Riihela, A., Mueller, R., Meirink, J. F., Sedlar, J., Stengel, M., Lockhoff, M., Trentmann,

962 J., Kaspar, F., Hollmann, R., and Wolters, E.: CLARA-A1: a cloud, albedo, and radiation dataset from

963 28 yr of global AVHRR data, Atmospheric Chemistry and Physics, 13, 5351-5367, 10.5194/acp-13-5351-

964 2013, 2013.

965 Kato, S., Loeb, N. G., Rutan, D. A., Rose, F. G., Sun-Mack, S., Miller, W. F., and Chen, Y.: Uncertainty

966 Estimate of Surface Irradiances Computed with MODIS-, CALIPSO-, and CloudSat-Derived Cloud and

967 Aerosol Properties, Surveys in Geophysics, 33, 395-412, 10.1007/s10712-012-9179-x, 2012.

968 Kato, S., Rose, F. G., Rutan, D. A., Thorsen, T. J., Loeb, N. G., Doelling, D. R., Huang, X., Smith, W. L.,

969 Su, W., and Ham, S.-H.: Surface Irradiances of Edition 4.0 Clouds and the Earth's Radiant Energy System

970 (CERES) Energy Balanced and Filled (EBAF) Data Product, J Climate, 31, 4501-4527, 10.1175/jcli-d-

971 17-0523.1, 2018a.

972 Kato, S., Rose, F. G., Rutan, D. A., Thorsen, T. J., Loeb, N. G., Doelling, D. R., Huang, X. L., Smith, W.

973 L., Su, W. Y., and Ham, S. H.: Surface Irradiances of Edition 4.0 Clouds and the Earth's Radiant Energy

974 System (CERES) Energy Balanced and Filled (EBAF) Data Product, Journal of Climate, 31, 4501-4527,

975 10.1175/Jcli-D-17-0523.1, 2018b.

Kato, S., Rose, F. G., Sun-Mack, S., Miller, W. F., Chen, Y., Rutan, D. A., Stephens, G. L., Loeb, N. G., Minnis, P., Wielicki, B. A., Winker, D. M., Charlock, T. P., Stackhouse, P. W., Xu, K.-M., and Collins, W. D.: Improvements of top-of-atmosphere and surface irradiance computations with CALIPSO-, CloudSat-, and MODIS-derived cloud and aerosol properties, Journal of Geophysical Research, 116, 10.1029/2011jd016050, 2011.

Kennedy, A., Xi, B., Dong, X., and Zib, B. J.: Evaluation and Intercomparison of Cloud Fraction and Radiative Fluxes in Recent Reanalyses over the Arctic Using BSRN Surface Observations, J Climate, 25, 2291-2305, 10.1175/jcli-d-11-00147.1, 2012.

Kenyon, J. S., Moninger, W. R., Smith, T. L., Peckham, S. E., Lin, H., Grell, G. A., Dowell, D. C., James, E. P., Olson, J. B., Smirnova, T. G., Alexander, C. R., Hu, M., Brown, J. M., Weygandt, S. S., Benjamin, S. G., and Manikin, G. S.: A North American Hourly Assimilation and Model Forecast Cycle: The Rapid Refresh, Mon Weather Rev, 144, 1669-1694, 10.1175/mwr-d-15-0242.1, 2016.

Kim, D. and Ramanathan, V.: Solar radiation budget and radiative forcing due to aerosols and clouds, Journal of Geophysical Research, 113, 10.1029/2007jd008434, 2008.

Kotarba, A. Z.: Evaluation of ISCCP cloud amount with MODIS observations, Atmos Res, 153, 310-317, 10.1016/j.atmosres.2014.09.006, 2015.

Kotarba, A. Z.: Calibration of global MODIS cloud amount using CALIOP cloud profiles, Atmospheric Measurement Techniques, 13, 4995-5012, 10.5194/amt-13-4995-2020, 2020.

Li, A., Bo, Y., Zhu, Y., Guo, P., Bi, J., and He, Y.: Blending multi-resolution satellite sea surface temperature (SST) products using Bayesian maximum entropy method, Remote Sensing of Environment, 135, 52-63, 10.1016/j.rse.2013.03.021, 2013.

Li, L., Shi, R., Zhang, L., Zhang, J., and Gao, W.: The data fusion of aerosol optical thickness using universal kriging and stepwise regression in East China, Conference on Remote Sensing and Modeling of Ecosystems for Sustainability XI, San Diego, CA, 2014

Aug 18-20, WOS:000344548600027, 10.1117/12.2061764, 2014.

Li, S. and Yang, B.: Multifocus image fusion by combining curvelet and wavelet transform, Pattern Recognition Letters, 29, 1295-1301, 10.1016/j.patrec.2008.02.002, 2008.

Liu, X., He, T., Sun, L., Xiao, X., Liang, S., and Li, S.: Analysis of Daytime Cloud Fraction Spatiotemporal Variation over the Arctic from 2000 to 2019 from Multiple Satellite Products, Journal of Climate, 35, 3995-4023, 10.1175/jcli-d-22-0007.1, 2022.

Liu, Y., Liu, S., and Wang, Z.: A general framework for image fusion based on multi-scale transform and sparse representation, Information Fusion, 24, 147-164, 10.1016/j.inffus.2014.09.004, 2015.

Liu, Y., Wu, W., Jensen, M. P., and Toto, T.: Relationship between cloud radiative forcing, cloud fraction and cloud albedo, and new surface-based approach for determining cloud albedo, Atmospheric Chemistry and Physics, 11, 7155-7170, 10.5194/acp-11-7155-2011, 2011a.

Liu, Y., Ackerman, S. A., Maddux, B. C., Key, J. R., and Frey, R. A.: Errors in Cloud Detection over the Arctic Using a Satellite Imager and Implications for Observing Feedback Mechanisms, Journal of Climate, 23, 1894-1907, 10.1175/2009jcli3386.1, 2010.

Liu, Y., Key, J. R., Liu, Z., Wang, X., and Vavrus, S. J.: A cloudier Arctic expected with diminishing sea

ice, Geophysical Research Letters, 39, n/a-n/a, 10.1029/2012gl051251, 2012a.

Liu, Y. H., Key, J. R., Ackerman, S. A., Mace, G. G., and Zhang, Q. Q.: Arctic cloud macrophysical characteristics from CloudSat and CALIPSO, Remote Sensing of Environment, 124, 159-173, 10.1016/j.rse.2012.05.006, 2012b.

Liu, Y. Y., Parinussa, R. M., Dorigo, W. A., De Jeu, R. A. M., Wagner, W., van Dijk, A. I. J. M., McCabe, M. F., and Evans, J. P.: Developing an improved soil moisture dataset by blending passive and active microwave satellite-based retrievals, Hydrology and Earth System Sciences, 15, 425-436, 10.5194/hess-15-425-2011, 2011b.

Loyola R, D. G., Thomas, W., Spurr, R., and Mayer, B.: Global patterns in daytime cloud properties derived from GOME backscatter UV-VIS measurements, Int J Remote Sens, 31, 4295-4318, 10.1080/01431160903246741, 2010.

Marchant, B., Platnick, S., Meyer, K., and Wind, G.: Evaluation of the MODIS Collection 6 multilayer cloud detection algorithm through comparisons with CloudSat Cloud Profiling Radar and CALIPSO CALIOP products, Atmospheric Measurement Techniques, 13, 3263-3275, 10.5194/amt-13-3263-2020, 2020.

Marchant, B., Platnick, S., Meyer, K., Arnold, G. T., and Riedi, J.: MODIS Collection 6 shortwave-derived cloud phase classification algorithm and comparisons with CALIOP, Atmos Meas Tech, 9, 1587-1599, 10.5194/amt-9-1587-2016, 2016.

Miao, Q. and Wang, B.: A Novel Image Fusion Method Using Contourlet Transform, International Conference on Communications,

Minnis, P., Sun-Mack, S., Young, D. F., Heck, P. W., Garber, D. P., Chen, Y., Spangenberg, D. A., Arduini, R. F., Trepte, Q. Z., Smith, W. L., Ayers, J. K., Gibson, S. C., Miller, W. F., Hong, G., Chakrapani, V., Takano, Y., Liou, K. N., Xie, Y., and Yang, P.: CERES Edition-2 Cloud Property Retrievals Using TRMM VIRS and Terra and Aqua MODIS Data-Part I: Algorithms, Ieee Transactions on Geoscience and Remote Sensing, 49, 4374-4400, 10.1109/tgrs.2011.2144601, 2011.

Nazelle, A. D., Arunachalam, S., and Serre, M. L.: Bayesian maximum entropy integration of ozone observations and model predictions: an application for attainment demonstration in North Carolina, Environ Sci Technol, 44, 5707-5713, 10.1021/es100228w, 2010.

Nie, S., Wu, T., Luo, Y., Deng, X., Shi, X., Wang, Z., Liu, X., and Huang, J.: A strategy for merging objective estimates of global daily precipitation from gauge observations, satellite estimates, and numerical predictions, Advances in Atmospheric Sciences, 33, 889-904, 10.1007/s00376-016-5223-y, 2016.

Paul, A. H.: Collection 6.1 Change Summary Document MODIS Atmosphere Level-3 Algorithm and Global Products, 2017.

Philipp, D., Stengel, M., and Ahrens, B.: Analyzing the Arctic Feedback Mechanism between Sea Ice and Low-Level Clouds Using 34 Years of Satellite Observations, Journal of Climate, 33, 7479-7501, 10.1175/jcli-d-19-0895.1, 2020.

Poulsen, C. J., Tabor, C., and White, J.: Response to Comment on "Long-term climate forcing by atmospheric oxygen concentrations", Science, 353, 10.1126/science.aad8550, 2016.

Qian, Y., Long, C. N., Wang, H., Comstock, J. M., McFarlane, S. A., and Xie, S.: Evaluation of cloud fraction and its radiative effect simulated by IPCC AR4 global models against ARM surface observations, Atmospheric Chemistry and Physics, 12, 1785-1810, 10.5194/acp-12-1785-2012, 2012.

Ramanathan, V., Cess, R. D., Harrison, E. F., Minnis, P., Barkstrom, B. R., Ahmad, E., and Hartmann, D.: Cloud-Radiative Forcing and Climate - Results from the Earth Radiation Budget Experiment, Science, 243, 57-63, DOI 10.1126/science.243.4887.57, 1989.

Rossow, W. B. and Schiffer, R. A.: Advances in understanding clouds from ISCCP, Bulletin of the American Meteorological Society, 80, 2261-2287, 10.1175/1520-0477(1999)080<2261:Aiucfi>2.0.Co;2, 1999.

Savelyeva, E., Utkin, S., Kazakov, S., and Demyanov, V.: Modeling Spatial Uncertainty for Locally Uncertain Data, 7th International Conference on Geostatistics for Environmental Applications, Southampton, ENGLAND, 2010

Sep, WOS:000288481100026, 295-+, 10.1007/978-90-481-2322-3_26, 2010.

Shupe, M. D., Turner, D. D., Walden, V. P., Bennartz, R., Cadeddu, M. P., Castellani, B. B., Cox, C. J., Hudak, D. R., Kulie, M. S., Miller, N. B., Neely, R. R., Neff, W. D., and Rowe, P. M.: HIGH AND DRY New Observations of Tropospheric and Cloud Properties above the Greenland Ice Sheet, B Am Meteorol Soc, 94, 169-+, 10.1175/Bams-D-11-00249.1, 2013.

Sledd, A. and L'Ecuyer, T. S.: Emerging Trends in Arctic Solar Absorption, Geophys Res Lett, 48, 10.1029/2021gl095813, 2021.

Spadavecchia, L. and Williams, M.: Can spatio-temporal geostatistical methods improve high resolution regionalisation of meteorological variables?, Agricultural and Forest Meteorology, 149, 1105-1117, 10.1016/j.agrformet.2009.01.008, 2009.

Stengel, M., Stapelberg, S., Sus, O., Schlundt, C., Poulsen, C., Thomas, G., Christensen, M., Carbajal Henken, C., Preusker, R., Fischer, J., Devasthale, A., Willén, U., Karlsson, K.-G., McGarragh, G. R., Proud, S., Povey, A. C., Grainger, R. G., Meirink, J. F., Feofilov, A., Bennartz, R., Bojanowski, J. S., and Hollmann, R.: Cloud property datasets retrieved from AVHRR, MODIS, AATSR and MERIS in the framework of the Cloud_cci project, Earth Syst Sci Data, 9, 881-904, 10.5194/essd-9-881-2017, 2017.

Stubenrauch, C. J., Rossow, W. B., Kinne, S., Ackerman, S., Cesana, G., Chepfer, H., Di Girolamo, L., Getzewich, B., Guignard, A., Heidinger, A., Maddux, B. C., Menzel, W. P., Minnis, P., Pearl, C., Platnick, S., Poulsen, C., Riedi, J., Sun-Mack, S., Walther, A., Winker, D., Zeng, S., and Zhao, G.: Assessment of Global Cloud Datasets from Satellites: Project and Database Initiated by the GEWEX Radiation Panel, Bulletin of the American Meteorological Society, 94, 1031-1049, 10.1175/bams-d-12-00117.1, 2013.

Sun, B. M., Free, M., Yoo, H. L., Foster, M. J., Heidinger, A., and Karlsson, K. G.: Variability and Trends in U.S. Cloud Cover: ISCCP, PATMOS-x, and CLARA-A1 Compared to Homogeneity-Adjusted Weather Observations, Journal of Climate, 28, 4373-4389, 10.1175/jcli-d-14-00805.1, 2015.

Tang, Q., Bo, Y., and Zhu, Y.: Spatiotemporal fusion of multiple-satellite aerosol optical depth (AOD) products using Bayesian maximum entropy method, Journal of Geophysical Research: Atmospheres, 121, 4034-4048, 10.1002/2015jd024571, 2016.

Tiedtke, M.: Representation of Clouds in Large-Scale Models, Monthly Weather Review, 121, 3040-3061, Doi 10.1175/1520-0493(1993)121<3040:Rocils>2.0.Co;2, 1993.

Toll, V., Christensen, M., Quaas, J., and Bellouin, N.: Weak average liquid-cloud-water response to anthropogenic aerosols, Nature, 572, 51-55, 10.1038/s41586-019-1423-9, 2019.

Trepte, Q. Z., Bedka, K. M., Chee, T. L., Minnis, P., Sun-Mack, S., Yost, C. R., Chen, Y., Jin, Z., Hong, G., Chang, F.-L., and Smith, W. L.: Global Cloud Detection for CERES Edition 4 Using Terra and Aqua MODIS Data, IEEE Transactions on Geoscience and Remote Sensing, 57, 9410-9449, 10.1109/tgrs.2019.2926620, 2019.

Tzallas, V., Hatzianastassiou, N., Benas, N., Meirink, J. F., Matsoukas, C., Stackhouse, P., and Vardavas, I.: Evaluation of CLARA-A2 and ISCCP-H Cloud Cover Climate Data Records over Europe with ECA&D Ground-Based Measurements, Remote Sens-Basel, 11, 10.3390/rs11020212, 2019.

Van Tricht, K., Lhermitte, S., Lenaerts, J. T. M., Gorodetskaya, I. V., L'Ecuyer, T. S., Noel, B., van den Broeke, M. R., Turner, D. D., and van Lipzig, N. P. M.: Clouds enhance Greenland ice sheet meltwater runoff, Nature Communications, 7, ARTN 10266

10.1038/ncomms10266, 2016.

Vaughan, M., Young, S., Winker, D., Powell, K., Omar, A., Liu, Z. Y., Hu, Y. X., and Hostetler, C.: Fully automated analysis of space-based lidar data: an overview of the CALIPSO retrieval algorithms and data products, Bba Lib, 5575, 16-30, 10.1117/12.572024, 2004.

Vaughan, M. A., Powell, K. A., Kuehn, R. E., Young, S. A., Winker, D. M., Hostetler, C. A., Hunt, W. H., Liu, Z. Y., McGill, M. J., and Getzewich, B. J.: Fully Automated Detection of Cloud and Aerosol Layers in the CALIPSO Lidar Measurements, Journal of Atmospheric and Oceanic Technology, 26, 2034-2050, 10.1175/2009jtecha1228.1, 2009.

Vignesh, P. P., Jiang, J. H., Kishore, P., Su, H., Smay, T., Brighton, N., and Velicogna, I.: Assessment of CMIP6 Cloud Fraction and Comparison with Satellite Observations, Earth and Space Science, 7, 10.1029/2019ea000975, 2020.

Walsh, J. E., Chapman, W. L., and Portis, D. H.: Arctic Cloud Fraction and Radiative Fluxes in Atmospheric Reanalyses, Journal of Climate, 22, 2316-2334, 10.1175/2008jcli2213.1, 2009.

Wang, D., Bi, S., Wang, B., and Yan, J.: Satellite cloud image fusion based on regional feature with nonsubsampled contourlet transform, Journal of Computer Applications, 32, 2585-2587, 2012.

Winker, D. M., Hunt, W. H., and McGill, M. J.: Initial performance assessment of CALIOP, Geophysical Research Letters, 34, Artn L19803

10.1029/2007gl030135, 2007.

Winker, D. M., Vaughan, M. A., Omar, A., Hu, Y. X., Powell, K. A., Liu, Z. Y., Hunt, W. H., and Young, S. A.: Overview of the CALIPSO Mission and CALIOP Data Processing Algorithms, Journal of Atmospheric and Oceanic Technology, 26, 2310-2323, 10.1175/2009jtecha1281.1, 2009.

Woodruff, S. D., Diaz, H. F., Worley, S. J., Reynolds, R. W., and Lubker, S. J.: Early ship observational data and ICOADS, Climatic Change, 73, 169-194, 10.1007/s10584-005-3456-3, 2005.

Wu, W., Liu, Y. G., Jensen, M. P., Toto, T., Foster, M. J., and Long, C. N.: A comparison of multiscale variations of decade-long cloud fractions from six different platforms over the Southern Great Plains in the United States, J Geophys Res-Atmos, 119, 3438-3459, 10.1002/2013jd019813, 2014.

Xia, X., Zhao, B., Zhang, T., Wang, L., Gu, Y., Liou, K.-N., Mao, F., Liu, B., Bo, Y., Huang, Y., Dong, J., Gong, W., and Zhu, Z.: Satellite-Derived Aerosol Optical Depth Fusion Combining Active and Passive Remote Sensing Based on Bayesian Maximum Entropy, IEEE Transactions on Geoscience and Remote Sensing, 60, 1-13, 10.1109/tgrs.2021.3051799, 2022.

Xie, S. C., McCoy, R. B., Klein, S. A., Cederwall, R. T., Wiscombe, W. J., Clothiaux, E. E., Gaustad, K. L., Golaz, J. C., Hall, S. D., Jensen, M. P., Johnson, K. L., Lin, Y. L., Long, C. N., Mather, J. H., McCord, R. A., McFarlane, S. A., Palanisamy, G., Shi, Y., and Turner, D. D. D.: ARM CLIMATE MODELING BEST ESTIMATE DATA A New Data Product for Climate Studies, Bulletin of the American Meteorological Society, 91, 13-+, 10.1175/2009bams2891.1, 2010.

Xu, S. and Cheng, J.: A new land surface temperature fusion strategy based on cumulative distribution function matching and multiresolution Kalman filtering, Remote Sensing of Environment, 254, 10.1016/j.rse.2020.112256, 2021.

Xu, S., Cheng, J., and Zhang, Q.: Reconstructing All-Weather Land Surface Temperature Using the Bayesian Maximum Entropy Method Over the Tibetan Plateau and Heihe River Basin, IEEE Journal of Selected Topics in Applied Earth Observations and Remote Sensing, 12, 3307-3316, 10.1109/jstars.2019.2921924, 2019.

Yang, J. and Hu, M.: Filling the missing data gaps of daily MODIS AOD using spatiotemporal interpolation, Science of the Total Environment, 633, 677-683, 10.1016/j.scitotenv.2018.03.202, 2018.

Yeo, H., Kim, M.-H., Son, S.-W., Jeong, J.-H., Yoon, J.-H., Kim, B.-M., and Kim, S.-W.: Arctic cloud properties and associated radiative effects in the three newer reanalysis datasets (ERA5, MERRA-2, JRA-55): Discrepancies and possible causes, Atmospheric Research, 270, 10.1016/j.atmosres.2022.106080, 2022.

Young, A. H., Knapp, K. R., Inamdar, A., Hankins, W., and Rossow, W. B.: The International Satellite Cloud Climatology Project H-Series climate data record product, Earth Syst Sci Data, 10, 583-593, 10.5194/essd-10-583-2018, 2018.

Yu, H.-L. and Wang, C.-H.: Retrospective prediction of intraurban spatiotemporal distribution of PM2.5 in Taipei, Atmospheric Environment, 44, 3053-3065, 10.1016/j.atmosenv.2010.04.030, 2010.

Zhang, C.-J., Chen, Y., Duanmu, C., and Feng, H.-J.: Multi-channel satellite cloud image fusion in the tetrolet transform domain, Int J Remote Sens, 35, 8138-8168, 10.1080/01431161.2014.980918, 2014.

Zhang, Q., Cheng, J., and Liang, S.: Deriving high-quality surface emissivity spectra from atmospheric infrared sounder data using cumulative distribution function matching and principal component analysis regression, Remote Sensing of Environment, 211, 388-399, 10.1016/j.rse.2018.04.033, 2018.

Zhu, X., Chen, J., Gao, F., Chen, X., and Masek, J. G.: An enhanced spatial and temporal adaptive reflectance fusion model for complex heterogeneous regions, Remote Sensing of Environment, 114, 2610-2623, 10.1016/j.rse.2010.05.032, 2010.